Volume 53
Number 22
21 November 2024
Pages 10793–11252

Chem Soc Rev

Chemical Society Reviews

rsc.li/chem-soc-rev

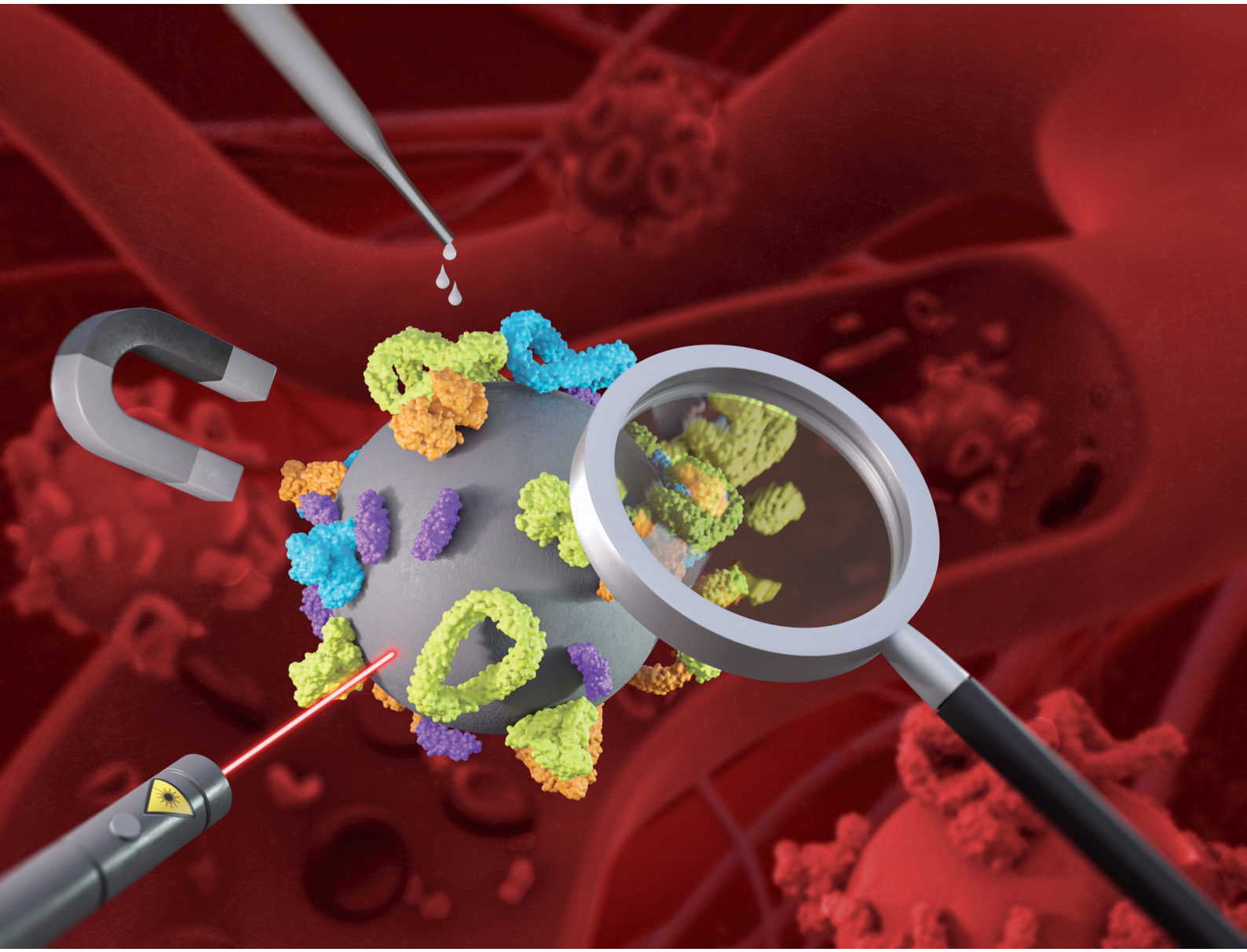

ISSN 0306-0012

ROYAL SOCIETY OF CHEMISTRY

TUTORIAL REVIEW

Katharina Landfester, Shuai Jiang *et al.*

In situ characterization techniques of protein corona around nanomaterials

Chem Soc Rev

TUTORIAL REVIEW

View Article Online
View Journal | View Issue

Cite this: *Chem. Soc. Rev.*, 2024, 53, 10827

In situ characterization techniques of protein corona around nanomaterials

Fangqin Fu,[ab] Daniel Crespy,[c] Katharina Landfester*[d] and Shuai Jiang*[ab]

Received 27th May 2024

DOI: 10.1039/d4cs00507d

rsc.li/chem-soc-rev

Nanoparticles (NPs) inevitably interact with proteins upon exposure to biological fluids, leading to the formation of an adsorption layer known as the "protein corona". This corona imparts NPs with a new biological identity, directly influencing their interactions with living systems and dictating their fates *in vivo*. Thus, gaining a comprehensive understanding of the dynamic interplay between NPs and proteins in biological fluids is crucial for predicting therapeutic effects and advancing the clinical translation of nanomedicines. Numerous methods have been established to decode the protein corona fingerprints. However, these methods primarily rely on prior isolation of NP–protein complex from the surrounding medium by centrifugation, resulting in the loss of outer-layer proteins that directly interact with the biological system and determine the *in vivo* fate of NPs. We discuss here separation techniques as well as *in situ* characterization methods tailored for comprehensively unraveling the inherent complexities of NP–protein interactions, highlighting the challenges of *in situ* protein corona characterization and its significance for nanomedicine development and clinical translation.

Key learning points

1. The concept of protein corona and its composition, biological impacts, and the challenges associated with its analysis.
2. Separation techniques for isolating nanoparticle-protein complexes from protein media and the separation mechanisms.
3. *In situ* characterization methods for protein corona analysis and their characterization mechanisms.

1. Introduction

Nanomedicines have drawn particular attention in cancer therapy due to their enhanced drug solubility, targeted delivery, and reduced systemic toxicity.[1,2] Considerable efforts have been devoted to advancing the clinical translation of nanomedicines. Up to now, only *ca.* 14 nano-formulations have received FDA approval for clinical anti-tumor practice. However, no active-targeting nanomedicines have progressed through clinical trials.[3] Indeed, the complex *in vivo* microenvironment and biological interactions present barriers to the clinical translation of nanomedicines.

Upon entering blood circulation, nanoparticles (NPs) inevitably interact with biomolecules, mainly proteins, resulting in the formation of protein corona that endows a new "biological identity" to the synthetic NPs. The unique protein corona fingerprint may lead to unpredictable effects on the *in vivo* fate of NPs,[4–6] such as the aggregation or destabilization of NPs,[7,8] opsonization that accelerates NP clearance from blood,[6,9–11] and potential immunological reactions due to interactions between NPs and immune cells.[12–14] Conversely, specific apolipoprotein adsorption can be advantageous for NPs' stealth behavior (by Apo A1 and clusterin)[15–17] and penetration of the blood–brain barrier (by Apo E).[18] Therefore, an in-depth understanding of NP–protein interactions is a prerequisite to reveal their biological effects and predict the *in vivo* fate of NPs.[19]

Protein corona formation is a thermodynamic and kinetic equilibrium process of protein adsorption and desorption.[20] Depending on the binding affinity and dissociation rate of proteins to NP surface, protein corona can be divided into "hard" corona (HC) and "soft" corona (SC).[21] The HC is

[a] *Key Laboratory of Marine Drugs, Chinese Ministry of Education, School of Medicine and Pharmacy, Ocean University of China, Qingdao 266003, China. E-mail: jiangshuai@ouc.edu.cn*
[b] *Laboratory for Marine Drugs and Bioproducts, Qingdao Marine Science and Technology Center, Qingdao 266237, China*
[c] *Department of Materials Science and Engineering, School of Molecular Science and Engineering, Vidyasirimedhi Institute of Science and Technology (VISTEC), Rayong 21210, Thailand*
[d] *Max Planck Institute for Polymer Research, Mainz 55128, Germany. E-mail: landfester@mpip-mainz.mpg.de*

composed of proteins with high binding affinity and low dissociation rate, tightly adsorbing on NP surface. Whereas the SC consists of proteins with low binding affinity and high dissociation rate, leading to their loose adhesion to NPs and continuous exchange with surrounding species. Notably, HC and SC are relative concepts based on protein binding affinity to NPs. Indeed, there are still no unified and specific methods to clearly distinguish SC from HC due to their unclear boundaries. The most common separation technique is centrifugation, and it is generally considered that SC can be removed from NPs after repeated washing by centrifugation. Although the general concepts of HC and SC are similar in different reports, varied compositions of HC and SC may obtain from different separation techniques.

The short residence time of SC proteins makes it challenging to distinguish them from free proteins in the medium. Conventional analysis methods of protein corona such as SDS-PAGE and LC-MS rely on isolation of the NP–protein complex from the medium by centrifugation, resulting in the loss of SC proteins that directly interact with the biological system and determines *in vivo* fate of NPs.[22,23] Hence the obtained compositions do not accurately reflect the real protein corona fingerprints. Therefore, scientific efforts have been made for developing either efficient isolation approaches that maximumly preserve the SC proteins or for developing *in situ* characterization techniques capable of directly detecting NP–protein interactions in biological medium without isolation.

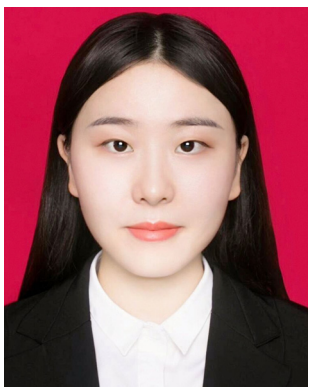

Fangqin Fu

Fangqin Fu obtained her Master degree in Pharmaceutics from Jinan University in China in 2022. She joined the group of Prof. Shuai Jiang at the Ocean University of China for her PhD thesis. Her research interests mainly focus on the influence of protein corona on the in vivo biofate of nanoparticles.

Daniel Crespy

Daniel Crespy studied Chemistry at the University of Strasbourg where he first came into contact with heterophase polymerizations. He joined Professor Katharina Landfester in 2003 to complete a PhD at the University of Ulm where he developed novel methods to prepare nanocapsules in miniemulsions. In 2006, he held a position as project leader at Empa, working on stimuli-responsive materials for textiles. He joined the department of Professor K. Landfester in the Max Planck Institute for Polymer Research in 2009 as group leader. Daniel Crespy is now Associate Professor since 2016 in the Vidyasirimedhi Institute of Science and Technology (VISTEC) in Thailand.

Katharina Landfester

Katharina Landfester received her Doctoral Degree in 1995. After a postdoctoral stay at the Lehigh University, she worked at the Max Planck Institute of Colloids and Interfaces leading the miniemulsion group. From 2003 to 2008, she was Full Professor at the University of Ulm. She joined the Max Planck Society in 2008 as one of the directors of the MPIP. She was awarded the Reimund Stadler prize of the German Chemical Society and the prize of the Dr Hermann Schnell Foundation. Her research focusses on creating functional colloids for new material and biomaterial applications.

Shuai Jiang

Shuai Jiang studied chemistry at Yantai University. He obtained his Doctoral Degree in 2016 in the Chinese Academy of Sciences. During his PhD, he worked with Prof. K. Landfester and Dr D. Crespy at the Max Planck Institute for Polymer Research through the CAS-MPG Doctoral Promotion Program. From 2016 to 2019, he conducted postdoctoral research with Prof. K. Landfester at the Max Planck Institute for Polymer Research. From 2019, he served as group coordinator for the Max Planck-VISTEC Laboratory for Sustained Materials. Since 2021, he is a Full Professor at the Ocean University of China. His research focuses on nanomedicines and nano-bio interactions.

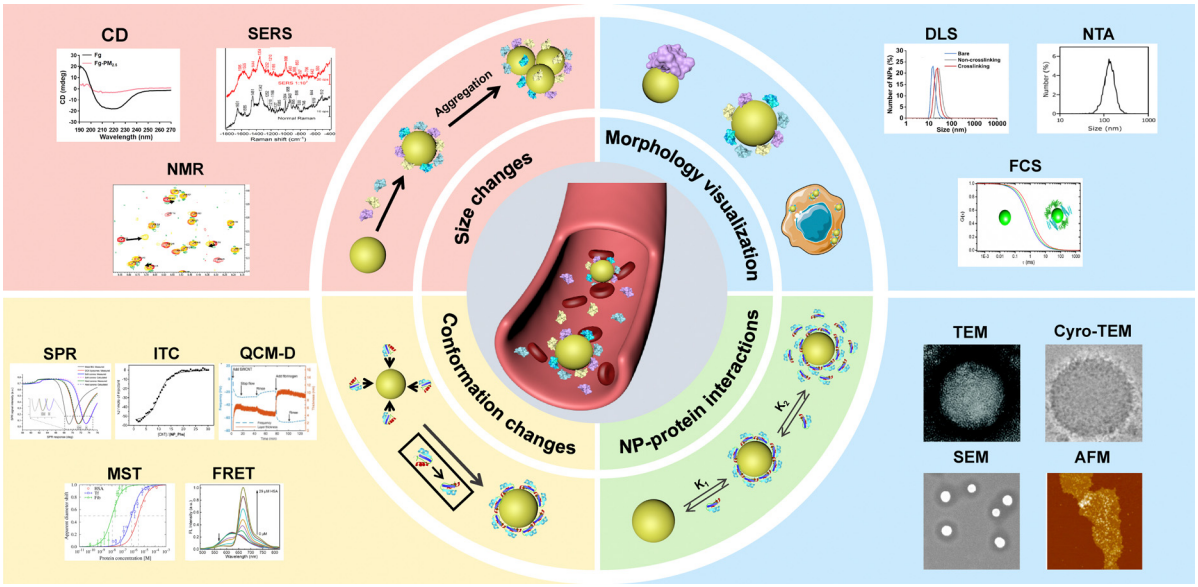

Fig. 1 *In situ* characterization techniques for analyzing protein corona around NPs. DLS result was reproduced from ref. 24 with permission from American Chemical Society. NTA result was reproduced from ref. 25 with permission from Elsevier Ltd. FCS result was reproduced from ref. 26 with permission from American Chemical Society. TEM result was reproduced from ref. 27 with permission from the Royal Society of Chemistry. Cryo-TEM result was reproduced from ref. 28 with permission from Nature Publishing Group. SEM result was reproduced from ref. 29 with permission from Elsevier Ltd. AFM result was reproduced from ref. 30 with permission from American Chemical Society. SPR result was reproduced from ref. 31 with permission from Controlled Release Society. ITC result was reproduced from ref. 32 with permission from American Chemical Society. QCM-D result was reproduced from ref. 33 with permission from Nature Publishing Group. MST result was reproduced from ref. 34 with permission from American Chemical Society. FRET result was reproduced from ref. 35 with permission from Wiley-VCH. CD result was reproduced from ref. 36 with permission from Elsevier Ltd. SERS result was reproduced from ref. 37 with permission from Frontiers. NMR result was reproduced from ref. 38 with permission from American Chemical Society.

In this review, we summarize the recent progress on separation techniques and *in situ* characterization methods for precise protein corona analysis. The separation techniques are systematically discussed and classified according to their mechanisms, including centrifugation, magnetic separation and chromatographic methods. *In situ* characterization methods are categorized based on the analytical purpose, including the size evolution of NPs, morphology of NP–protein complex, kinetics of NP–protein interactions, conformation changes of proteins, as well as composition of the protein corona (Fig. 1).

2. Separation techniques for isolating NP–protein complex from protein media

Isolation of the NP–protein complex from the biological fluids is often required for *ex situ* analysis of protein corona. The composition of obtained protein corona could be further analyzed with protein identification techniques such as LC-MS and SDS-PAGE. However, the separation procedure critically affects the obtained composition of protein corona due to the loss of loosely bound proteins. The most commonly used separation techniques for isolating NP–protein complexes are centrifugation, magnetic separation and chromatographic methods.

2.1 Centrifugation

Centrifugation is the most commonly applied separation technique for isolating NP–protein complexes,[39,40] relying on the density and size differences between NPs and free proteins. It is considered an efficient means of isolating tightly adsorbed proteins on the NPs.[23] The sedimentation velocity V of spherical NPs with a diameter D can be described by the Stokes equation (eqn (1)):[41]

$$V = \frac{1}{18} \cdot \frac{(\rho - \rho_0) \cdot g}{\eta} \cdot D^2 \quad (1)$$

with ρ and ρ_0 being the densities of NPs and centrifugation medium, g is the gravitational force and η is the viscosity of the medium. According to the Stokes equation, the sedimentation rate is proportional to the square of NP diameter, resulting in a significant difference in sedimentation rate between NPs and free proteins. Moreover, significant differences in densities enhance the efficiency of separation. For example, the densities of silica NPs and AuNPs are ~2.20 and 19.30 g cm^{-3}, respectively, while human serum albumin has a density of 0.99 g cm^{-3}.[42,43]

The composition of obtained corona proteins is significantly influenced by centrifugation parameters such as force, duration, and cycles. Increasing the number of washing cycles led to the elimination of loosely bounded proteins, favoring the

formation of HC rather than SC.[44] Studies have revealed that low abundance proteins such as apolipoprotein A1 and antithrombin-III became enriched in the protein corona as the number of washing cycles increased from 1 to 3. This enrichment occurred due to the easier removal of loosely bounded SC proteins, thereby concentrating the low abundance yet high affinity proteins within the obtained HC corona.[45] Additionally, false positive or false negative outcomes may arise from simultaneous precipitation of free proteins or protein aggregates together with the NP–protein complexes, or detachment of loosely bound proteins.[46] Recent reports indicate that a substantial amount of albumin, the most abundant protein in plasma and serum, tends to sediment during the centrifugation process for isolating the liposome–protein corona complexes.[47] Moreover, the medium solutions used for protein corona preparation also affect the composition results. Brückner *et al.*[48] compared eight different solutions and found that the obtained corona composition was dramatically affected by the washing solutions. For instance, when water was employed as a washing medium, there was an enrichment in immunoglobulins, a phenomenon not observed with other aqueous solutions. Conversely, washing with Dulbecco's Modified Eagle Medium (DMEM) favored a strong binding of serum albumin. These distinct protein corona signatures may stem from alterations in protein structure induced by variation of pH and osmotic pressure of the diverse washing media. Böhmert *et al.*[49] systematically reviewed studies on the critical centrifugation parameters such as rotational velocity, time, and temperature, in protein corona study (Fig. 2). They concluded that these parameters should be considered in a holistic view. For specific NPs and given biological medium, the centrifugation parameters must be optimized in order to acquire accurate information.

Advanced centrifugation approaches such as using sucrose cushions and ultracentrifugation have been employed for protein corona isolation. A sucrose cushion improves centrifugation separation efficiency by stratifying the sample components based on their buoyant densities.[50] This is achieved by creating a density gradient with sucrose, wherein sucrose's higher density relative to the samples allows for more precise fractionation. Unbound proteins in the incubation media can be separated from the NPs and agglomerates by the sucrose cushion method.[51,52] For the NPs with low density, ultracentrifugation is a suitable approach to achieve high separation efficiency. However, NPs and proteins may aggregate upon the high centrifugation force (commonly above 100 000 g). Therefore, it can be applied jointly with a sucrose gradient cushion for better separation efficiency.[53,54] Multiple centrifugation and purification steps may result in SC loss and disrupt the adsorption equilibrium of corona proteins.

2.2 Magnetic separation

Magnetic separation is an important technique for preparing protein corona of magnetic NPs (*e.g.*, iron oxide NPs).[55]

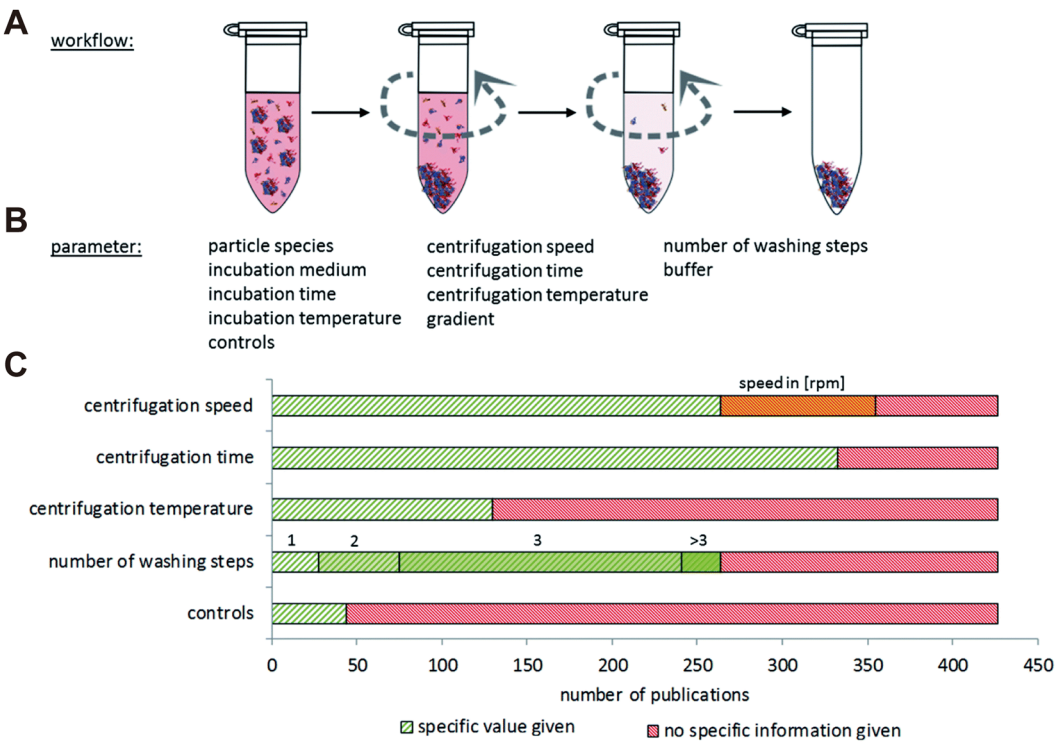

Fig. 2 Overview of NP separation methodology based on centrifugation. (A) General procedure of centrifugation comprising repeated washing and centrifugation steps. (B) Main parameters related to centrifugation techniques for protein corona analysis. (C) Number of literatures involving the study on centrifugation speed, centrifugation time, centrifugation temperature, number of washing steps and controls. Green: the specific information is given in the publication; red: no specific information is given in the publication; orange: only the rpm values are given in the publication but not the exact centrifugation force.[49] Reproduced from ref. 49 with permission from the Royal Society of Chemistry.

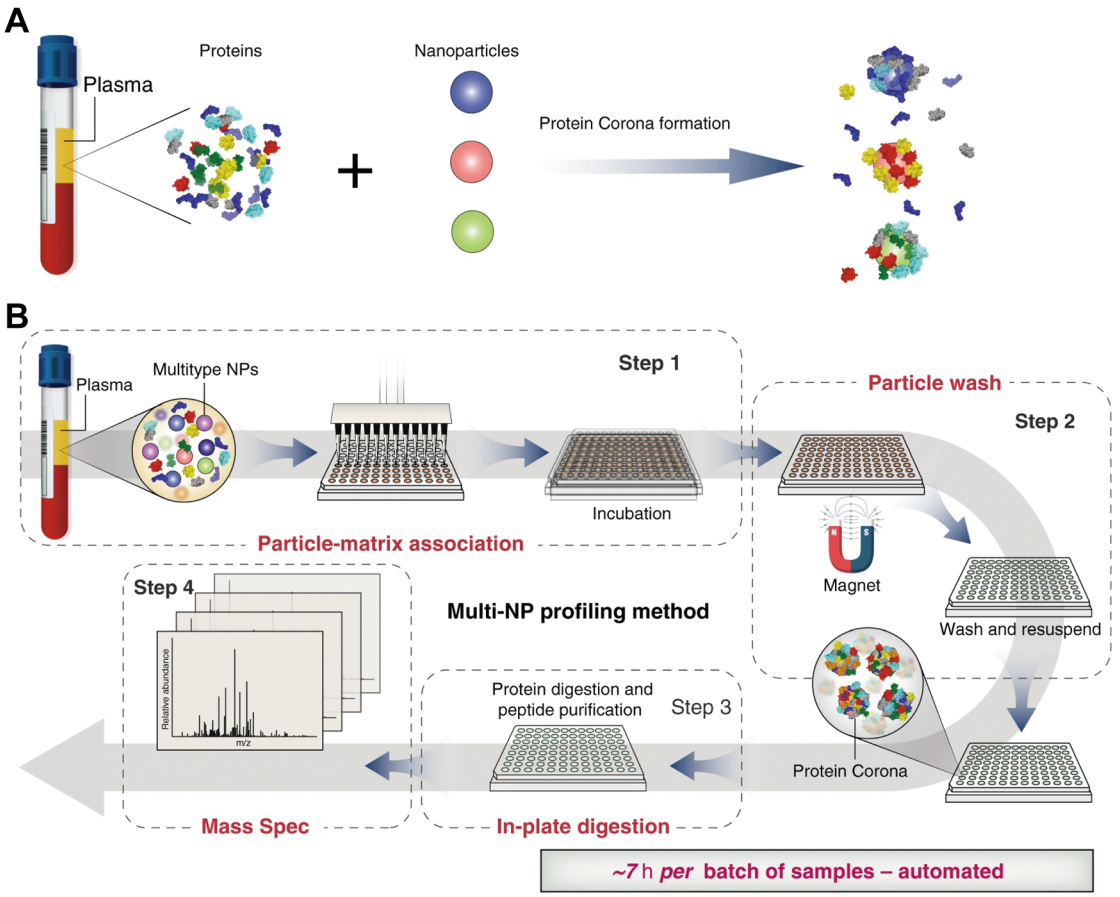

Fig. 3 (A) Incubation of NPs with different physicochemical properties (indicated by different colors) in blood plasma results in different protein corona compositions. (B) Proteograph platform workflow based on multi-NP protein corona approach and mass spectrometry for plasma proteome analysis. The proteograph workflow includes four steps: (1) NP-plasma incubation and protein corona formation; (2) NP protein corona purification by a magnet; (3) digestion of corona proteins; and (4) LC-MS/MS analysis. In this context, each plasma-NP well is a sample, for a total of 96 samples per plate.[59] Reproduced from ref. 59 with permission from Nature Publishing Group.

Compared with centrifugation, the magnetic separation process is relatively mild and capable of selectively isolating the NP–protein complex from its mixture with biological fluids components such as blood cells and biomolecules.[56] Hoang *et al.*[57] compared the composition of protein corona obtained by centrifugation and magnetic separation. It was found that more proteins were lost during centrifugation compared to magnetic separation. The magnetic force facilitated the removal of more hydrophilic proteins by overcoming van der Waals forces between proteins and NPs, whereas the intensive centrifugal force was able to overcome electrostatic attraction forces between proteins and NPs, resulting in the removal of more positively charged proteins. Similarly, Bonvin *et al.*[58] investigated the influence of centrifugation and magnetic separation methods on the HC composition. They found that magnetic separation dramatically reduced the content of false-positive proteins resulting from protein aggregation during centrifugation process. Moreover, Blume *et al.*[59] developed a multiple magnetic NPs-based protein separation method that relies on the differential interactions of distinct NPs with proteins (Fig. 3). Therefore, employing multiple NPs with distinct surface properties could enhance proteomic sampling and yield more comprehensive proteomics data. Nevertheless, magnetic separation cannot function as a universal method for protein corona preparation due to the limitation of NP types, *i.e.* they must be superparamagnetic and responsive to an external magnetic field. Additionally, such an automated method may introduce protein contamination due to protein adsorption from plasma to the well plates. Moreover, as the size of NPs increases, agglomeration occurs during magnetic separation. Therefore, NPs with diameters larger than 10 nm are not suitable for the magnetic separation.

Magnetic levitation (MagLev) has been utilized to investigate the heterogeneity of protein corona surrounding NPs.[60] Unlike conventional magnetic separation, the measured NPs do not require responsiveness to magnetic fields. The principle relies on the dispersion of diamagnetic objects, such as diamagnetic NPs, in a paramagnetic medium under a non-homogenous magnetic field. The diamagnetic object, provided that the difference of magnetic susceptibilities between diamagnetic object and surrounding paramagnetic medium is negative, will levitate at a position depending on its density.[50] Owing to the

difference in density between bare NPs and NPs coated with protein corona, a variation of protein corona composition on a sole population of NPs was observed, corresponding to different levitation height and hence revealing heterogeneities of protein corona.[61] However, it remains unclear whether the paramagnetic medium influences the composition of the protein corona.

2.3 Chromatographic methods

Chromatographic methods, including asymmetric-flow-field-flow-fractionation (AF4), size exclusion chromatography (SEC), capillary electrophoresis (CE)[62–64] and hydrodynamic chromatography (HDC),[65] have been utilized for isolating NP–protein corona complexes. Chromatographic methods effectively separate different species based on their hydrodynamic sizes, enabling the determination of protein affinity to NPs and the association/dissociation rates of proteins with NPs. Compared with centrifugation and magnetic separation, chromatographic separation offers a milder process that minimizes perturbation of protein corona. However, the chromatographic separation methods are usually time-consuming and costly.

SEC is a conventional chromatography method that separates species based on their hydrodynamic volumes.[66–70] The stationary phase of SEC is filled with porous beads that allow small species to enter the pore cavity, while larger species are eluted first by the mobile phase. NPs with tightly adsorbed proteins are eluted faster than bare NPs due to the increased size, whereas NPs with lower protein affinity result in easy dissociation of proteins from NPs and therefore are eluted at similar times as bare NPs. This separation mechanism enables to determine association and dissociation rates of proteins. However, the interactions of corona proteins with stationary phase may reduce the separation efficiency. Additionally, the shear stress occurring between the NP, protein corona and stationary phase may lead to the detachment of loosely bound proteins, consequently altering the corona composition.[71,72] Besides, it is found that unbound free proteins can co-elute with liposomes during SEC isolation of liposome–protein complexes. Notably, a comparison of isolation methods including SEC, centrifugation and membrane ultrafiltration revealed that SEC is susceptible to co-eluting PEGylated liposomes with other free proteins, leading to contamination of the protein corona.[25]

Field flow fractionation (FFF) is a flow-assisted separation technique designed for samples with a molar weight lower than 10^{15} g mol^{-1},[73] specifically for fractionating materials of nanoscale dimensions.[74] Unlike traditional chromatography methods such as SEC, FFF does not use a stationary phase, which helps to avoid unwanted interactions between samples and the stationary phase.[75] Instead, solutes are fractionated within layers of a continuous flow, directed by an external field perpendicular to the direction of the mobile phase. FFF offers significant advantages over other chromatography methods, particularly in reducing shearing force and accurately analyzing complex mixtures and fragile samples, such as aggregates.[76] AF4 is a mild separation technique suitable for separating biological substances within the size range of 1 nm to 1 μm.[77] The AF4 channel consists of a porous wall on one side, forming a perpendicular force to the sample flow that forces sample separation (Fig. 4).[78–80] Species with different diffusion coefficients can be effectively separated, with smaller substances eluting faster than larger ones.[81] Compared with other conventional chromatographic methods, AF4 replaces traditional gel permeation columns with a hollow channel without the stationary phase, thereby minimizing nonspecific interactions of proteins with the column materials. Moreover, the low shear forces of AF4 can minimize the perturbation to the protein corona composition.[82,83] Weber *et al.*[84] compared the protein corona patterns of polystyrene NPs obtained from centrifugation and AF4. Their results revealed that human serum albumin (HSA), typically associated with NPs as a soft corona protein, was identified as a major component in the protein corona following AF4 separation, whereas only a minimal amount of HSA was detected in the protein corona after centrifugation. These results implied that the AF4 is suitable for isolating SC proteins without disturbing the weak interactions of NPs with low affinity proteins. Although AF4 provides a mild and efficient way to isolate NP–protein complex and meanwhile preserves the SC, the establishment of AF4 methodology is usually time-consuming owning to its multiple parameters to be optimized. Moreover, the adsorption of sample to the membrane of AF4 channels has also to be considered.

Collectively, a range of separation techniques have been developed to achieve comprehensive isolation of the protein corona while minimizing the loss of its components.

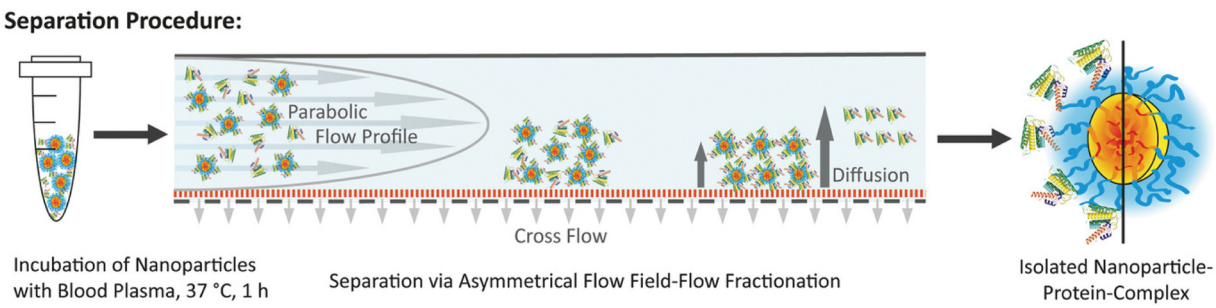

Fig. 4 Schematic illustration of the separation process of NP–protein complex from unbound proteins *via* AF4 and the isolated NP–protein complex.[80] Reproduced from ref. 80 with permission from Wiley-VCH.

Table 1 Overview of the different protein corona separation techniques

Techniques	Advantages	Disadvantages
Centrifugation	Commonly available Economical applicability High throughput[85]	Long centrifugation times Disturbing NP–protein interaction
Magnetic separation	Economical applicability High throughput	Only for magnetic NPs with diameter less than 10 nm[58]
Chromatographic methods	Short measurement time[78,84] Reduced perturbation of protein composition	Expensive Long time to establish standard process

Nonetheless, these techniques inevitably disrupt the formation and composition of protein corona to varying degrees, leading to potential inaccuracies such as false positives or false negatives. Table 1 provides a comprehensive overview of the diverse separation techniques discussed in this review.

2.4 New techniques for protein corona separation

To overcome the dilemma of traditional separation methods, considerable efforts have been devoted to develop mild and specific techniques for efficient isolation of protein corona. Mohammad-Beigi *et al.*[86] developed a novel separation technique based on strain-promoted alkyne azide cycloaddition (SPAAC) "click" chemistry (Fig. 5). This capture process enabled the identification of weakly interacting proteins along with the long-lived protein corona forming around NP in complex media. Specifically, silica and polystyrene NPs were first incubated with fetal bovine serum (FBS) to form NP-HC complexes after centrifugation. Then, the NP-HC and FBS (to form SC layer) was separated modified to carry $-N_3$ and –DBCO groups, enabling a spontaneously click-chemistry reaction after incubation. SC proteins can be then covalently captured for further proteomic analysis. Proteomic results showed that most of captured proteins are present in both SC and HC, indicating that the same proteins can have both high and low binding affinities to NPs. This click chemistry-based method is highly versatile for the separation of protein coronas across various NPs. However, chemical modification of proteins may alter their characteristics and adsorption profiles. The modified chemical identities, *i.e.*, $-N_3$ and –DBCO groups, may also contribute to the interaction of NP-HC with SC proteins.

Due to their stereo-selective surfaces, chiral nanomaterials have been found to induce distinct biological responses including cellular uptake, energy metabolism, and cell differentiation.[87] Baimanov and co-workers[88] established a bio-layer interferometry (BLI)-based fishing strategy for real-time monitoring of the dynamic interactions of chiral NPs with serum proteins (Fig. 6). Specifically, IgG was initially immobilized on an amine-reactive 2nd generation biosensor (AR2G) capable of reacting with protein or peptides containing primary amine groups, followed by the binding of chiral Cu_2S NPs (L-NPs and D-NPs) *via* their high binding affinity to the IgG. The obtained chiral biosensors were exposed to 10% mouse serum at 37 °C under continuous shaking of the microplate. Protein adsorption on NPs was monitored in real-time by measuring the change of wavelength shift ($\Delta\lambda$) in the biosensor, which reflects changes in bio-layer thickness due to protein adsorption. The SC and HC proteins were obtained through sequential washing steps and further subjected to LC-MS/MS analysis. The results showed that the chirality of Cu_2S NPs dramatically affected the composition of SC and HC proteins, leading to distinct blood clearance profiles of NPs. In comparison with the SC of L-NPs, more opsonin proteins were detected in the SC of D-NPs that resulted in shorter blood circulation. This fishing strategy enables real-time detection of the evolution of HC and SC on NPs and reveals subtle difference in NP–protein interactions even within several minutes. However, the binding of IgG and Cu_2S NPs may reduce the contact area of NPs with serum proteins, therefore reducing the number of adsorbed proteins and altering their spatial distribution. To generalize this BLI-based fishing strategy for different NPs,

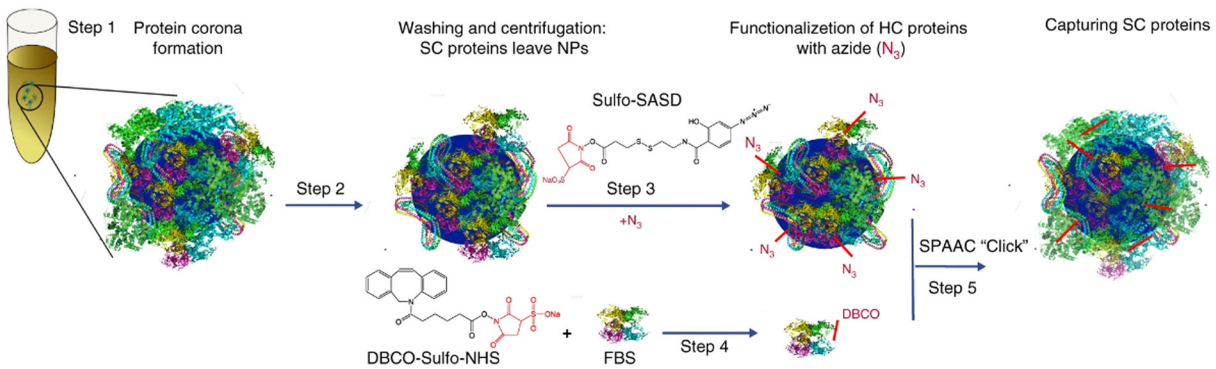

Fig. 5 Schematic representation of capturing SC proteins. After protein corona formation (steps 1 and 2), the HC proteins were modified with N_3 by reacting with sulfo-SASD (step 3) followed by a SPAAC "click" reaction (step 5) with FBS-D proteins (prepared in step 4).[86] Reproduced from ref. 86 with permission from Nature Publishing Group.

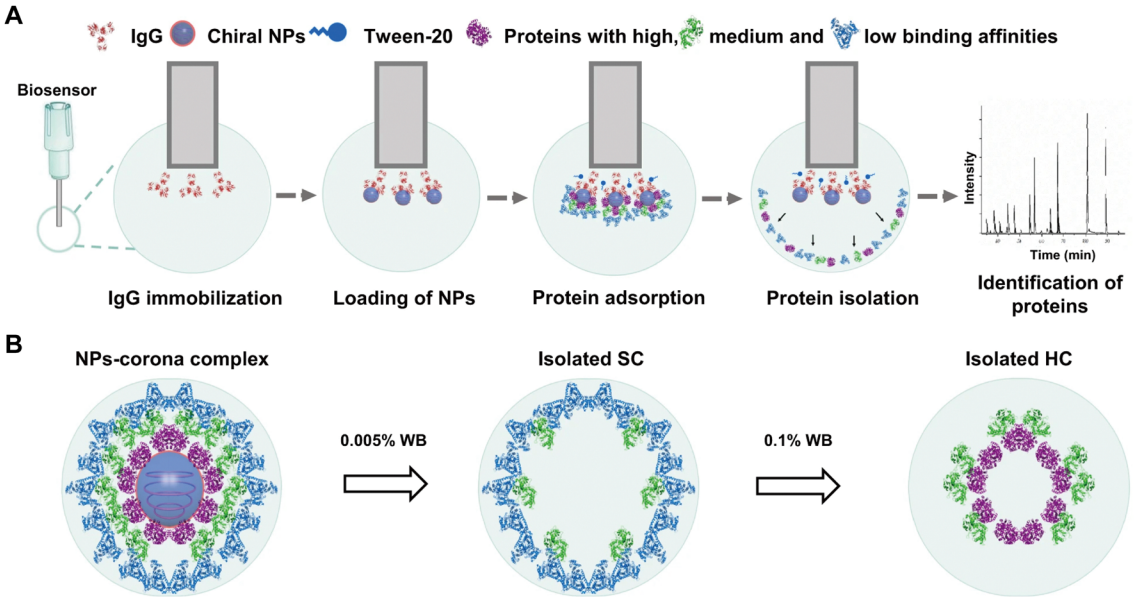

Fig. 6 Schematic illustration of BLI-based fishing strategy including protein corona formation on the chiral NPs, isolation of corona, and identification of protein composition and abundance. (A) The whole method includes five steps: (1) coating of the biosensors with IgG; (2) loading of chiral NPs onto the biosensors; (3) incubation of NPs with biological fluids and formation of protein corona; (4) isolation of protein coronas from the NPs; (5) protein digestion and proteomic analysis for identification of corona components by LC–MS/MS. (B) Isolation process of NPs-corona complex. The spherical structures with gray blue and blue colors refer to Cu_2S NPs and Tween-20 (a surfactant), respectively; while the irregular structures with purple, green, light blue, and red colors represent various types of proteins.[88] Reproduced from ref. 88 with permission from Nature Publishing Group.

systematic screening of high-affinity proteins specific to each NP is required.

Chu and co-workers[89] developed an affinity chromatography (AfC) method using His-tagged anti-PEG single-chain variable fragment (PEG-scFv) for efficient and specific separation of protein corona formed on the PEGylated liposomes (sLip) (Fig. 7). In this method, the His-tagged PEG-scFv could readily capture sLip without affecting protein corona compositions, while also separating the sLip/protein complexes from plasma protein aggregates and endogenous vesicles through the Ni-NTA column. Briefly, the PEG-scFv was tagged with His tag for binding on the Ni-NTA column. Upon exposure in a sLip-protein solution, the His-tagged PEG-scFv successfully capture the sLip-protein complexes through specific binding of antigen (PEG on sLip) with antibody (PEG-scFv). Therefore, the protein corona on sLip can be separated from unbound free proteins, protein aggregates, and other endogenous vesicles. The AfC displayed a 43-fold increase of *in vitro* protein corona

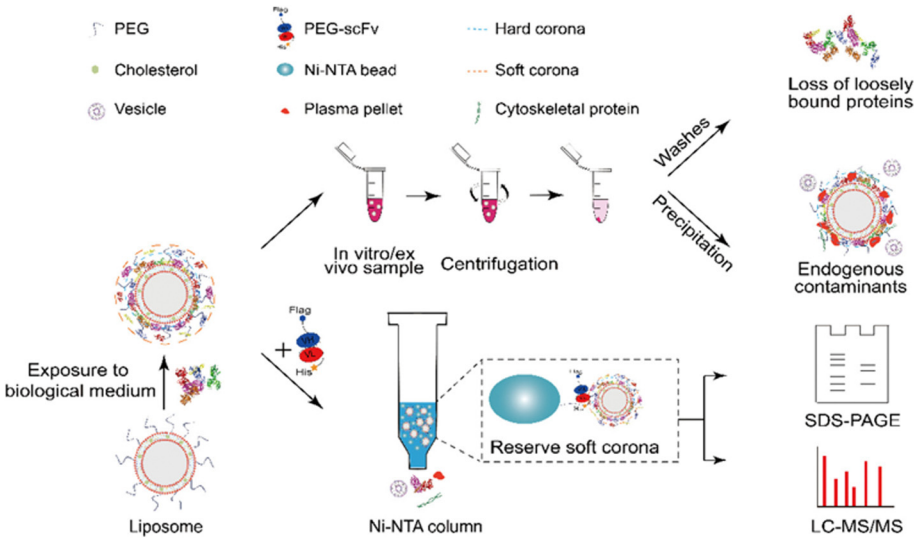

Fig. 7 Schematic illustration of the separation procedures of protein corona by affinity chromatography (lower row) and comparison with centrifugation (upper row).[89] Reproduced from ref. 89 with permission from American Chemical Society.

separation efficiency compared to centrifugation. This method avoided contamination from protein aggregates and endogenous vesicles occurring during centrifugation and effectively reserved the loosely bounded SC proteins due to the mild separation condition. Collectively, the AfC provides an unprecedented approach for deeply deciphering protein coronas and is suitable for separating *in vivo* protein coronas due to its high specificity and minimal sample volume requirement. However, this method is only applicable to the PEGylated samples, constraining its scope of application. Moreover, the protein corona may shield the binding of PEG chains to the PEG-scFv on the column.

Table 2 provides a comprehensive overview of the diverse separation techniques discussed in this review. While the delicate design of these novel methods enhances the efficiency and specificity of protein corona preparation, they also face several challenges. Often, they require complex preparatory procedures or expensive materials, impeding their universal applications. For instance, the BLI-based fishing strategy is applicable only to Cu2S NPs due to their high affinity to IgG. To broaden its application, it is essential to explore proteins with high affinity for other types of NPs, such as lipid, polymer, and silica NPs. The AfC method, based on PEG-scFv, is currently limited to separating protein coronas on PEGylated NPs. Given that PEGylation is a common modification in nanomedicine, this approach holds promise as a versatile method. Furthermore, by leveraging diverse antigen–antibody interactions, this method could be extended to other functionalized NPs, such as those modified with antibodies or glycosylation. Collectively, advancing towards direct measurement methods that circumvent the challenges of the separation step represents a promising strategy for protein corona studies.

3. *In situ* characterization methods of protein corona

In situ characterization directly measures the NP–protein interactions in biological media without the need of an extra separation step for isolating the NP–protein complexes. Therefore the disturbance of NP–protein interactions and the loss of weakly adsorbed SC proteins during the separation procedure can be avoided.[90–92] Classical *in situ* characterization methods include dynamic light scattering (DLS),[24,93] fluorescence correlation spectroscopy (FCS),[94,95] transmission electron microscopy (TEM),[96] circular dichroism (CD) spectroscopy,[97,98] and isothermal titration calorimetry (ITC), *etc.*[99,100] These methods provide insights into the size and morphology of NP–protein complexes, the quantity, kinetics, and affinity of NP–protein interactions, as well as the conformational changes of proteins upon adsorption.

3.1 Characterization methods for the size of NP–protein complex

Determining the size change of NPs after their incubation with proteins or in other biological media can reveal the protein adsorption and aggregation state of NPs. Common methods for this analysis include DLS, FCS, nanoparticle tracking analysis (NTA), and diffusion ^{19}fluorine-magnetic resonance (^{19}F-NMR) spectroscopy.

3.1.1 DLS. DLS measures the apparent diffusion coefficient of NP–protein complex through fluctuations in scattered light and further translates it into hydrodynamic radius *via* the Stokes–Einstein equation (eqn (2)):[101,102]

$$D = \frac{k_B T}{6\pi\eta R_h} \quad (2)$$

where D is the translational diffusion coefficient of NPs in a fluid and k_B is the Boltzmann constant. T is the temperature of the fluid and η represents the viscosity of the fluid. R_h is the hydrodynamic radius of the NPs.[103] Casals *et al.*[104] used DLS to measure the size change of Au NPs after incubation with a cell culture medium supplemented with serum. They found that the hydrodynamic diameter of Au NPs increased from 10 nm to 16 nm upon the incubation. Rausch *et al.*[105] investigated the aggregation status of PEGylated poly-*l*-lysines (PLL-*g*-PEOx) with various PEGylation degrees after incubation with human serum by using DLS. Aggregates with sizes of a few hundred nanometers were observed in the mixtures of serum and PLL-*g*-PEOx with a PEGylation degree $<10\%$. However, no aggregates were detected when the PEGylation degree exceeded 20%. Nevertheless, unbounded proteins in the medium may interfere with the scattering signal of NP–protein complex.

To eliminate background signals from unbound proteins, Balog *et al.*[106] applied the depolarized dynamic light scattering (DDLS) to investigate size changes of differently PEGylated Au NPs (coated with PEG-NH_3^+, PEG-COO^-, or PEG-CH_3) after incubation in common biological fluids (Fig. 8A). Owing to their polycrystalline nature, spherical metallic NPs (*e.g.*, Au and

Table 2 Overview of the new techniques for protein corona separation

Techniques	Advantages	Disadvantages
Click chemistry-based strategy	Wide applicability High sensitivity Simple operation process	Chemical modification may affect intrinsic characteristics and adsorption profiles of proteins
BLI-based fishing strategy	High sensitivity Real-time monitoring of the protein corona evolution Protein corona evolution	Costly and time-consuming Only for Cu_2S NPs with high binding affinity to IgG
Affinity chromatography	Mild separation condition High specificity Reduced perturbation of protein composition and protein contamination	Complex preparatory procedures Expensive Only applicable to PEGylated samples

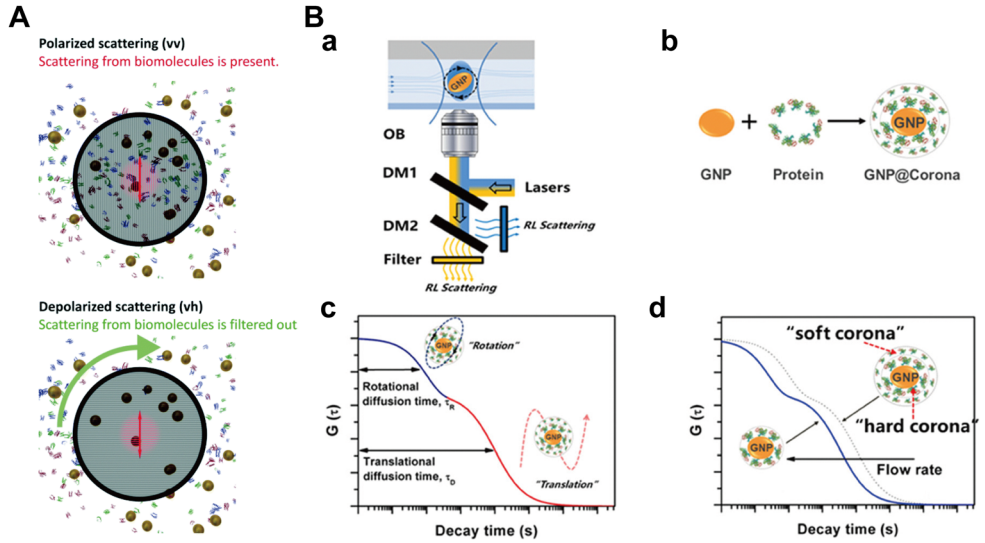

Fig. 8 (A) Standard polarized (top) and depolarized (down) DLS experiments. In the polarized scattering experiment scattering from the biomolecules is present, while it is invisible in the depolarized scattering experiment and thus can be ignored compared to the depolarized scattering from the NPs. Therefore, scattering exclusively from the NPs on an essentially zero background is detected in the depolarized scattering experiment.[106] Reproduced from ref. 106 with permission from the Royal Society of Chemistry. (B) Detection of protein corona formation *in situ* by D-RLSCS; (a) schematic illustration of D-RLSCS system measuring gold NPs (GNPs) in a microfluidic channel; (b) formation of protein corona on the surface of GNPs; (c) the curve of D-RLSCS consisting of rotational and translational diffusion of GNPs with protein corona; (d) D-RLSCS curves of GNPs with protein corona flowed in the microchannel varied with flow rate.[107] Reproduced from ref. 107 with permission from the Royal Society of Chemistry.

Ag NPs) exhibit an internally heterogeneous structure and deviate slightly from perfect sphericity, resulting in a subtle yet significant optical anisotropy. When excited by electromagnetic waves, the Au NPs support the coherent oscillation of the surface conduction electrons, known as localized surface plasmon resonance (LSPR). Upon scattering, the LSPR coupled with inherent optical anisotropy of Au NPs leads to a depolarized speckle pattern, whose temporal fluctuations of NPs can yield information about the size of Au NPs. Contrasted with the depolarized scattering of Au NPs, the depolarized scattering arising from biological matrices, such as unbounded proteins and lipids, was almost negligible and can be disregarded. The finding demonstrated that the sizes of PEG-COO^- and PEG-CH_3 coated Au NPs remained unchanged after incubation with all tested fluids (including PBS, bovine serum albumin (BSA) in PBS, DMEM, and 10% FBS in DMEM), indicating their low affinity to the protein molecules. Conversely, the size of PEG-NH_3^+ coated Au NPs increased by approximately 14 nm when exposed to the BSA solution, implying a strong interaction between the NPs and BSA. The DDLS efficiently mitigated irrelevant signals within complex environments, enabling real-time quantitative measurements of Au NP–protein complexes with an unprecedented signal-to-noise ratio. Nonetheless, this approach is limited to spherical metallic NPs characterized by a polycrystalline structure, such as Au NPs, Ag NPs, and Cu NPs.

3.1.2 NTA. In addition to the previously mentioned DLS and FCS, NTA has also been utilized as a complementary method for detecting size changes of NPs upon protein interactions. NTA monitors the Brownian motion of individual NPs in liquids by analyzing their scattered light, and subsequently correlates this motion with NPs size using the Stokes–Einstein equation.[108–111] Compared to DLS, NTA is more suitable for detecting polydisperse samples with high resolution, and the presence of small amounts of large (1000 nm) NPs generally does not compromise the accuracy of NTA measurements.[112] This characteristic enables the measurement of interactions between NPs and biological fluids.[113] For instance, Hajdú and colleagues[114] examined the alterations in the size of SPIONs post-incubation with human plasma using NTA and DLS. The NTA results revealed the formation of relatively monodisperse protein-SPION complexes in human plasma, characterized by larger hydrodynamic sizes and lower zeta potentials compared to the pristine NPs, which correlated with the findings from DLS. Owing to the intricate composition of serum samples, conventional DLS and NTA analysis in scattering mode cannot selectively detect the NPs. However, employing NTA analysis in fluorescence mode enables specific tracking of the motion of fluorescently labeled NPs. In a study conducted by Jeong and colleagues, the formation of protein corona in different media (*i.e.*, single protein solution and serum) and its effect on change of sizes of PEGylated doxorubicin-loaded liposomes were directly detected using fluorescence-nanoparticle tracking analysis without prior isolation of the NPs.[115] The NTA results clearly demonstrated that PEG density on liposome surface dramatically influenced the corona formation, leading to pronounced protein adsorption on liposomes with low PEGylation density compared to those with high PEGylation density. These results underscore the advantage of NTA in fluorescence mode for probing the natural protein corona formation in complex biological environments compare to DLS. However, NTA requires additional optimization steps and relies on user

experimentation for parameter settings, hindering its broader adoption.

3.1.3 FCS. FCS is a fluorescence-based technique. It determines the diffusion coefficient of fluorescent species through measuring fluctuations in fluorescence intensity in a small area of a sample, and further translates it into hydrodynamic radius.[26,116,117] Therefore, FCS can detect signals emitted from the fluorescently-labelled NPs or the NP–protein complexes with minimal interference from unbound proteins in biological fluids. Using FCS, Pelaz *et al.*[118] conducted *in situ* measurements to assess change in the effective hydrodynamic radius of NPs upon the adsorption of HSA and fibrinogen (FIB). The NPs without PEG modification exhibited a thickness increase of *ca.* 3 nm, corresponding to adsorption of a monolayer of HSA at high HSA concentration. In comparison, PEGylated NPs exhibited only a modest size increase of about 1.5 nm. Although this increase indicated the formation of protein corona, fluorescence lifetime and quenching analyses suggest that the adsorbed proteins are buried within the PEG shell. The change in NP diameter was less pronounced for FIB adsorption compared to HSA, likely due to the enhanced penetration of FIB molecules and subsequent deformation of the PEG layer.

However, the application of FCS for *in situ* measurements in blood is limited by pronounced absorption and scattering of light by blood components (*e.g.*, cells and proteins) in the visible spectrum where conventional FCS setups and common fluorescent labels operate. Negwer *et al.*[119] addressed this limitation by either labeling NPs or loading cargos with near-infrared (NIR) dyes with excitation and emission wavelengths falling within the range of 700–1100 nm. This range corresponds to the so-called NIR window in biological tissue, wherein light exhibits maximal penetration depth. Utilizing NIR labels and fitting the experimental autocorrelation functions with an analytical model that considers the presence of blood cells, they successfully monitored the size and drug loading of NPs in the blood, achieving sensitivity down to single dye molecule level. This technique enabled the investigation of protein corona formation on NPs within flowing blood. While the translational diffusion of NPs determined by FCS is directly proportional to particle size, the rotational diffusion coefficient of NPs exhibits a proportionality to the cube of particle size. This implies that the rotational diffusion of NPs should exhibit greater sensitivity to size changes than their translational diffusion. However, extracting this parameter poses challenges due to the high rotation rate and subtle optical signal fluctuations in conventional methods, resulting in diminished sensitivity to NP–protein binding. Moreover, introducing a fluorescence label on either the NPs or the proteins may alter their properties and hinder accurate measurement of rotational diffusion.

To overcome this issue, Zhang *et al.*[107] proposed a dual-wavelength laser-irradiated differenced resonance light scattering correlation spectroscopy (D-RLSCS) technique, combined with the modified generation method of the D-RLSCS curve to *in situ* investigate the protein corona formation on the label-free NPs. Specifically, the dissociation constants and binding rates of proteins, including BSA and FIB, to gold nanosheets were determined by analyzing the binding-induced ratiometric diffusion changes of NPs (the ratio of characteristic rotational diffusion time to translational diffusion time) (Fig. 8B). The results showed that BSA exhibits stronger binding constant and faster binding rate to gold nanosheets compared with FIB. In contrast to conventional methods such as FCS, this novel D-RLSCS strategy provides comprehensive insights into protein corona by averaging the diffusion behavior of numerous NPs. Besides, it effectively mitigates the impact of increased viscosity resulting from the high concentration of proteins.

^{19}F-NMR spectroscopy has also been utilized to detect size changes of the NP–protein complex. Diffusion ^{19}F-NMR measures the diffusion coefficient of ^{19}F-labeled NPs by identifying the chemical shift of ^{19}F resulting from the protein binding, and then converts it to the diameter of NPs using the Stokes–Einstein equation (eqn (2)).[120] Owing to its non-optical nature and the absence of interfering fluorinated molecules in physiological media, the ^{19}F-NMR spectroscopy can be applied in turbid environments, even in the presence of cells. For example, Carril and co-workers[121] employed ^{19}F-NMR spectroscopy to determine alterations in the hydrodynamic radius of fluorinated PEG-labeled Au NPs with different head groups (–COOH and –NH_2) and surface coating (poly(isobutylene-*alt*-maleic anhydride), PMA) in complex media. The results indicated that all three types of NPs remained colloidally stable and well dispersed in blood and plasma, without any detected agglomeration. NP-F/NH_2@PMA exhibited a size increase of approximately 5.5 nm after plasma incubation, while the size of NP-F/COOH and NP-F/NH_2 decreased due to the shrinkage of the PEG-containing ligands in plasma. These results illustrated the suitability of ^{19}F-NMR for *in situ* analysis of protein corona formation without any purification. However, ^{19}F-NMR spectroscopy results highly depend on the concentration of fluorine atoms. The presence of fluorine head groups on NPs can repel proteins and may hence affect their adsorption. Specifically, the hydrophobic nature of fluorine head groups can affect interactions with proteins like fibrinogen. Moreover, larger-sized NPs may experience increased mobility constraints, leading to limitations in accurately detecting diffusion coefficients. Additionally, evaluating interactions between proteins and NPs with soft coatings, such as PEG, presents challenges due to the inherent shrinkage and compressibility of these coatings.

3.2 Characterization methods for the morphology of NP–protein complex

Imaging techniques, notably transmission electron microscopy (TEM), cryogenic transmission electron microscopy (Cryo-TEM), scanning electron microscopy (SEM), and atomic force microscopy (AFM), serve as intuitive and compelling means for characterizing protein corona formation on NPs.[122–124] These methods are instrumental in providing a comprehensive understanding of the morphology, protein binding forms, and aggregation state of the NP-corona complexes.[125–127]

3.2.1 TEM. TEM is well-suited for visualizing the morphology and intricate microstructures of NPs at the nanometer

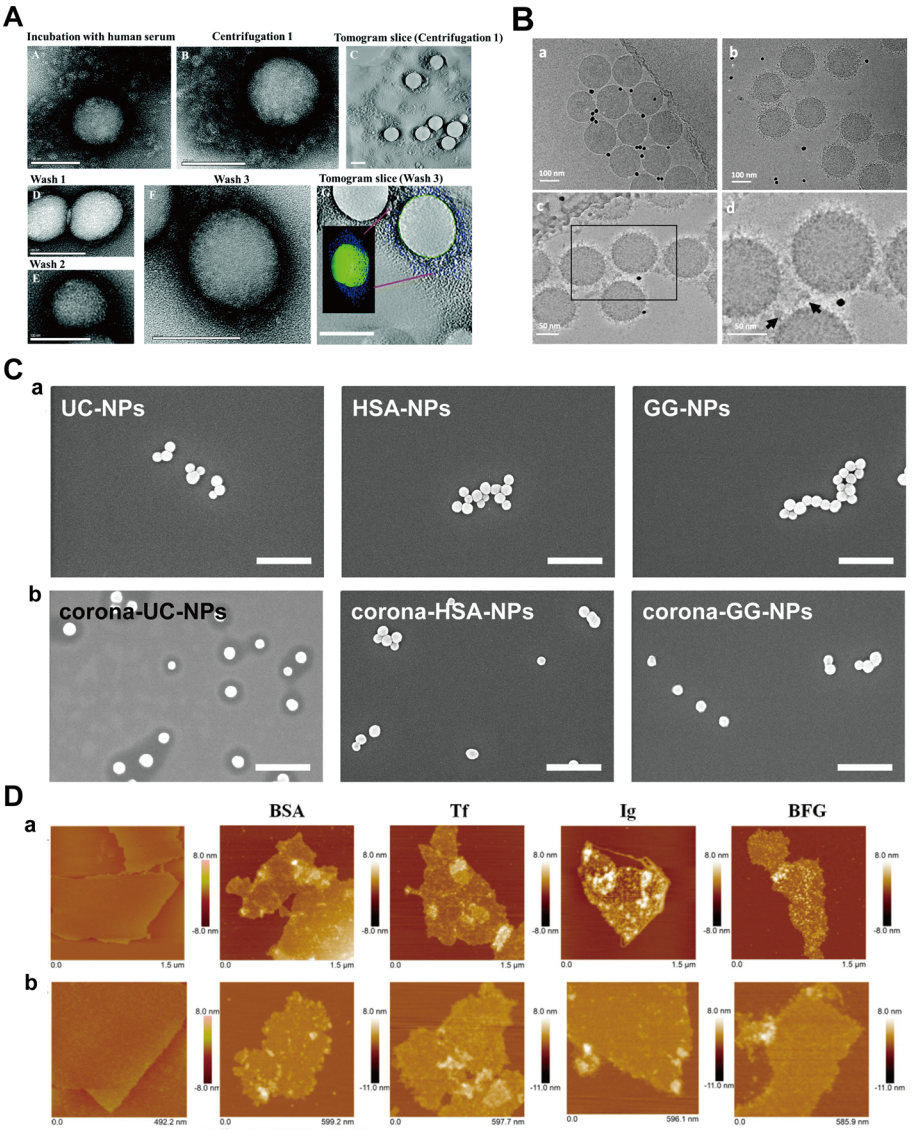

Fig. 9 (A) TEM images of protein corona surrounding polystyrene NPs; (a) HC and SC of polystyrene NPs in human serum. (b) HC and SC of NPs after centrifugation and removal of the supernatant, but before washing steps. (c) Tomogram slice of the area in (b). (d) and (e) HC obtained after 1st wash, after 2nd wash, and after 3rd wash, respectively. (g) Electron tomogram slice of the area presented in (f). Scale bar: 100 nm.[27] Reproduced from ref. 27 with permission from the Royal Society of Chemistry. (B) Cryo-TEM images of polystyrene NPs; TEM images of (a) bare NPs without corona and (b) NPs with corona; (c) and (d) Distribution of proteins and their association with NP surface at higher magnification. Black dots in the images are 10 nm gold fiducial markers. The arrows indicate proteins accumulated between NPs as large clusters.[28] Reproduced from ref. 28 with permission from Nature Publishing Group. (C) SEM images of silica NPs; (a) SEM images and (b) corresponding size distribution of uncoated NPs and NPs pre-coated with HSA and γ-globulin; (c) SEM images and (d) corresponding size distribution plots of corona-coated NPs. Scale bars are 500 nm.[29] Reproduced from ref. 29 with permission from Elsevier Ltd. (D) Morphology of GO-protein complexes by AFM; AFM images of bare-GO (first column) and GO-protein complexes after incubation of BSA, Tf, Ig, or BFG with GO for 5 min (a) and 60 min (b).[30] Reproduced from ref. 30 with permission from American Chemical Society.

scale. Al-Ahmady *et al.*[128] employed TEM to examine the structural integrity and morphology of protein-coated thermosensitive liposomes, revealing the evident presence of protein corona on the liposome surface. Kokkinopoulou *et al.*[27] employed TEM to visualize the process of protein corona formation, starting from the initial incubation of polystyrene NPs with human serum and continuing through subsequent washing/centrifugation steps. The images showed that the protein corona constitutes an undefined and loose protein network, rather than the conventional perception of a dense protein shell (Fig. 9A). Despite the advantages of TEM for directly visualizing protein corona formation and structures, the use of non-specific heavy metal staining to enhance the contrast of protein molecules for imaging may potentially disrupt the proteins' secondary structure, leading to artifacts and potentially misleading conclusions.[129]

3.2.2 Cryo-TEM. Cryo-TEM, a powerful imaging technique applied at cryogenic temperatures, enables high-resolution 3D reconstructions of biomolecules in near-native states, thereby facilitating the precise elucidation of their complex molecular

architectures critical for comprehending their functions and interactions. Franqui *et al.*[130] utilized cryo-TEM to investigate the interaction of graphene oxides (GOs) with a cell culture medium (*i.e.*, DMEM) by evaluating protein corona formation in fetal bovine serum (FBS). The study revealed an increased electronic density across the hard corona-coated GO sheets compared to the bare GO, indicating the adsorption of FBS onto the GO. To visualize the biomolecules within the corona and their association with the surface of polystyrene NPs, Sheibani *et al.*[28] developed a combined approach comprising cryo-electron microscopy, cryo-electron tomography, and three-dimensional reconstruction. Their findings revealed the detailed morphology and nanoscale distribution of the protein corona on the NP surface, showing a random distribution of clusters of proteins and other biomolecules from the plasma (Fig. 9B). Despite its advantages of high-resolution observation in the near-native states, the limited accessibility of cryo-TEM measurement due to costly equipment and demanding sample preparation requirements constrains its widespread application.

3.2.3 SEM. SEM employs a focused beam of electrons to create highly detailed images of samples surfaces, allowing for high-resolution visualization of their shape, texture, and composition at the micro- and nanoscale. The difference between SEM and TEM imaging lies in their distinct image formation methods: SEM utilizes reflected electrons for image generation, whereas TEM relies on electrons passing through the material for observeation.[131] Consequently, SEM can offer a more comprehensive 3D surface morphology image of the NP–protein complex compared to TEM and cryo-TEM. Using SEM, Mirshafiee *et al.*[29] investigated the alterations of morphology and size of silica NPs after pre-incubation with proteins (Fig. 9C). SEM images revealed that pre-coating with HSA or γ-globulin increased the size of silica NPs by approximately 5 or 9 nm, respectively, along with the formation of small NP aggregates. Nevertheless, visualizing the morphology of NPs with bound proteins is highly complex and necessitates the coordination of multiple characterization techniques to acquire comprehensive and reliable information.[132]

3.2.4 AFM. AFM, characterized by high resolution, low invasiveness, and minimal destructiveness, is another useful analysis technique for determining sizes, aggregation state, and surface roughness of the NP–protein complex.[133] Applying AFM, Chong *et al.*[30] investigated adsorption of BSA, immunoglobulin (Ig), transferrin (Tf), and bovine fibrinogen (BFG) on GO nanosheets. AFM images revealed diverse adsorption behaviors of the proteins on the GO surface (Fig. 9D). Specifically, BSA and Tf formed complex aggregates on the GO sheets that showed minimal changes during the incubation period. In contrast, Ig and BFG initially displayed uniform adsorption on the GO surface, which gradually transitioned into large aggregates over time, indicating a heterogeneous adsorption pattern. Kim *et al.*[134] observed an increase in size and a more round morphology of DNA tetrahedron with trivalent cholesterol conjugation ($Chol_3$-Td) following its incubation with high-density lipoprotein (HDL) and low-density lipoprotein (LDL) as revealed by AFM. Although AFM can provide insights into the actual state of NPs and allow the visualization of the protein corona, discerning the formation of hard or soft corona on NPs can be challenging. Moreover, the repeatability of AFM measurements depends on precise calibration of multiple parameters, including tip's shape, cantilever spring constant, and optical lever sensitivity.[135]

While electron microscopic techniques offer valuable insights into the morphology of protein corona, they also present inherent challenges. The high vacuum conditions during sample preparation at room temperatures, required for sample drying, poses a risk of introducing artifacts and the formation of large aggregates. Moreover, high protein concentrations in biological fluids can lead to significant background levels.[136] Hence, these techniques are typically used as complementary methods of *in situ* characterization of the protein corona.

3.3 Characterization of the kinetics of NP–protein interactions

Monitoring NP–protein interactions in the bloodstream is of crucial importance for comprehending the *in vivo* behavior of nanomedicines administered intravenously. Key methods for studying the kinetics of NP–protein interactions include surface plasmon resonance (SPR),[137–139] isothermal titration calorimetry (ITC),[140–142] quartz crystal microbalance with dissipation monitoring (QCM-D),[143,144] microscale thermophoresis (MST),[145] and fluorescence resonance energy transfer (FRET).[146,147]

3.3.1 SPR. Based on the propagation of surface plasmons on a metal surface upon light excitation, SPR allows sensitive and label-free monitoring of NP–protein interactions. NPs are immobilized on a dedicated biosensor surface, followed by an injection of protein solutions or biological fluids onto the biosensor surface. Protein binding to NPs is monitored through changes in the oscillation of surface plasmon wave on the biosensor chip.[148,149] Notably, SPR not only detects protein binding affinity to NPs but also provides real-time association/dissociation kinetics with minimal sample quantities in a label-free setting.[150] The equations describing the real-time SPR response at any time t in the dissociation phase R_d and the real-time SPR response at any time t in the association phase R_a are:[151]

$$R_d = A \cdot e^{-k_d \cdot t} + R_{d_0} \quad (3)$$

$$R_a = A_2 - A_3 \cdot e^{-(C \cdot k_a + k_d) \cdot t} \quad (4)$$

where R_{d_0} is the response at the start of the dissociation phase, A is the slope of the fitting curve for the dissociation phase, A_2 and A_3 represent the intercept and slope of the fitting curve for the association phase, respectively. C is the concentration of proteins while k_a and k_d are the association and dissociation constants, respectively.

Kari *et al.*[31] utilized multi-parametric SPR (MP-SPR) to monitor protein corona formation and determine the affinity (K_D) of C3b with liposomes in undiluted human serum. Their

observations revealed formulation-dependent HC and SC with distinct refractive indices, layer thicknesses, and surface mass densities (Fig. 10A). Upon serum injection, a SC with a thickness of 38–87 nm was formed on DOX liposomes, while the layer thickness on DOX + PEG liposomes was slightly thinner (26–60 nm). After washing with buffer, a significantly thinner HC layer remained on the surface of DOX liposomes compared to the DOX + PEG liposomes (3–7 *vs.* 8–13 nm). Moreover, the K_D values were 3.8×10^{-8} M and 7.2×10^{-8} M for the interaction of C3b with DOX liposomes and DOX + PEG liposomes, respectively. Miclăuş *et al.*[152] introduced an LSPR technique for quantifying both SC and HC formation on polyvinylpyrrolidone (PVP)-stabilized silver nanocubes (AgNCs). This method capitalizes on the sensitivity of the LSPR phenomenon of AgNCs to the surrounding refractive index due to coherent oscillation of surface conduction electrons, enabling a precise quantification of protein binding to the NPs. Their findings demonstrated a significantly elevated protein presence in SC compared to HC at all time points (with an 8-fold difference under 10% serum conditions), highlighting the sensitivity of SPR in probing interaction dynamics. Nevertheless, the relatively high cost and the need to tailor SPR biosensors for individual NPs limit the universal applicability of SPR.[92] Additionally, the detection limit of SPR is relatively high, *e.g.*, 1–10 nM for proteins with molecular weight smaller than 20 KDa.

3.3.2 ITC. ITC, a nondestructive method for *in situ* analyzing biochemical thermodynamics, monitors the time-dependent heat evolution and provides incremental heat as a function of the protein-to-NP molar ratio. Apart from evaluating the chemometrics of protein binding and NP–protein affinity, ITC yields essential thermodynamic parameters like Gibbs free energy (ΔG), enthalpy (ΔH), and entropy (ΔS) in real-time, enabling the interpretation of the intensity and types of interactions between proteins and NPs.[153–157] The corresponding equation is shown below:[158]

$$\Delta G = \Delta S - T\Delta H = -RT\ln K \quad (5)$$

where ΔG, ΔS, and ΔH represent the Gibbs free energy change, enthalpy change, and entropy change during protein–NP interaction, respectively. K is the associative binding constants corresponding to temperature (T), and R is the gas constant.

De *et al.*[32] investigated the interaction of Au NPs bearing various L-amino acid functionalities with α-chymotrypsin (ChT), histone and cytochrome *c* (CytC), and quantified their binding thermodynamics by ITC. The obtained thermodynamic parameters (ΔG, ΔH, and ΔS) revealed significant variations in the interaction mode between Au NPs and different proteins. The binding of NPs with ChT was an enthalpy-driven process, whereas binding with histones and CytC was driven by entropy (Fig. 10B). Yin *et al.*[159] studied the mechanism of interaction between gold nanoclusters functionalized with dihydrolipoic acid (DHLA-AuNCs) with HSA and Tf. The results corroborated that the interaction of DHLA-AuNCs with HSA was an endothermic dynamic process, while it exhibited an exothermic static process with Tf. Besides, ΔH and ΔS associated with the interaction of DHLA-AuNCs with HSA were found to be approximately 64 kJ mol^{-1} and 327 J mol^{-1} K^{-1}, respectively. In contrast, ΔH and ΔS for DHLA-AuNCs-Tf interactions were about −5 kJ mol^{-1} and 74 J mol^{-1} K^{-1}, respectively. The positive ΔS values indicate that the interactions between DHLA-AuNCs and both proteins are entropy-driven, which is attributed to desolvation of water molecules during hydrophobic interactions. However, potential aggregation of NPs due to concentrated samples required for ITC measurements and thermal perturbations caused by protein denaturation could potentially lead to misleading outcomes. Therefore, integrating complementary methods becomes imperative to validate ITC results and retrieve additional insights into the nature of the interactions.

3.3.3 QCM-D. QCM-D evaluates NP–protein interactions by measuring the total mass change resulting from adsorbed proteins, with a sensitivity ranging from micrograms to nanograms.[160,161] This methodology involves immobilizing NPs on an oscillating quartz surface, which exhibits high sensitivity to mass changes. Upon protein adsorption, QCM-D can ascertain the mass adsorption, adsorption mechanism, and protein thickness by monitoring alterations in resonant frequency and damping.[162,163] The deposition or adsorption of proteins results in a decrease of resonance frequency (Δf) of QCM-D, which can be correlated with the mass added (Δm) according to the Sauerbrey equation:[164]

$$\Delta m = -C \cdot \frac{\Delta f}{n} \quad (6)$$

where Δm is the areal mass (the mass adsorbed on the surface of quartz crystal, ng) or mass variation over the sensor surface (ng cm^{-2}), and C is the mass sensitivity factor. $C = 17.7$ ng cm^{-2} Hz^{-1} for a quartz crystal with a fundamental resonance of 5 MHz. When driven by an alternating current, the mass sensor of QCM-D oscillates at both its fundamental and overtone resonance frequencies. n is the overtone number and Δf is the frequency shift (Hz) measured for the selected harmonic n.

Bisker *et al.*[33] monitored the adsorption of fibrinogen onto DPPE-PEG5k-labeled single-wall carbon nanotubes (SWCNTs) on a gold-coated crystal, and subsequently determined the resulting layer thickness. The adsorption process, as evidenced by a gradual decrease in the crystal's oscillation frequency (Fig. 10C), suggested an increase in layer thickness. Upon measurement, it was revealed that a fibrinogen monolayer (approximately 5 nm thick) was attached to the top of the SWCNTs, implying a parallel alignment of the protein's long axis with the nanotube surface. Kaufman *et al.*[163] investigated the adsorption of BSA, CytC, and myoglobin (Mb) onto mercaptoundecanoic acid-stabilized Au NPs using QCM-D. The results indicated the formation of adsorption layers for all three proteins, consisting of both reversibly and irreversibly adsorbed fractions. BSA exhibited the highest affinity for AuNPs, forming a rigid, irreversibly adsorbed monolayer with a side-down orientation. The irreversibly adsorbed fraction of CytC exhibited a monolayer structure, whereas that of Mb displayed a bilayer. Nevertheless, the presence of water and

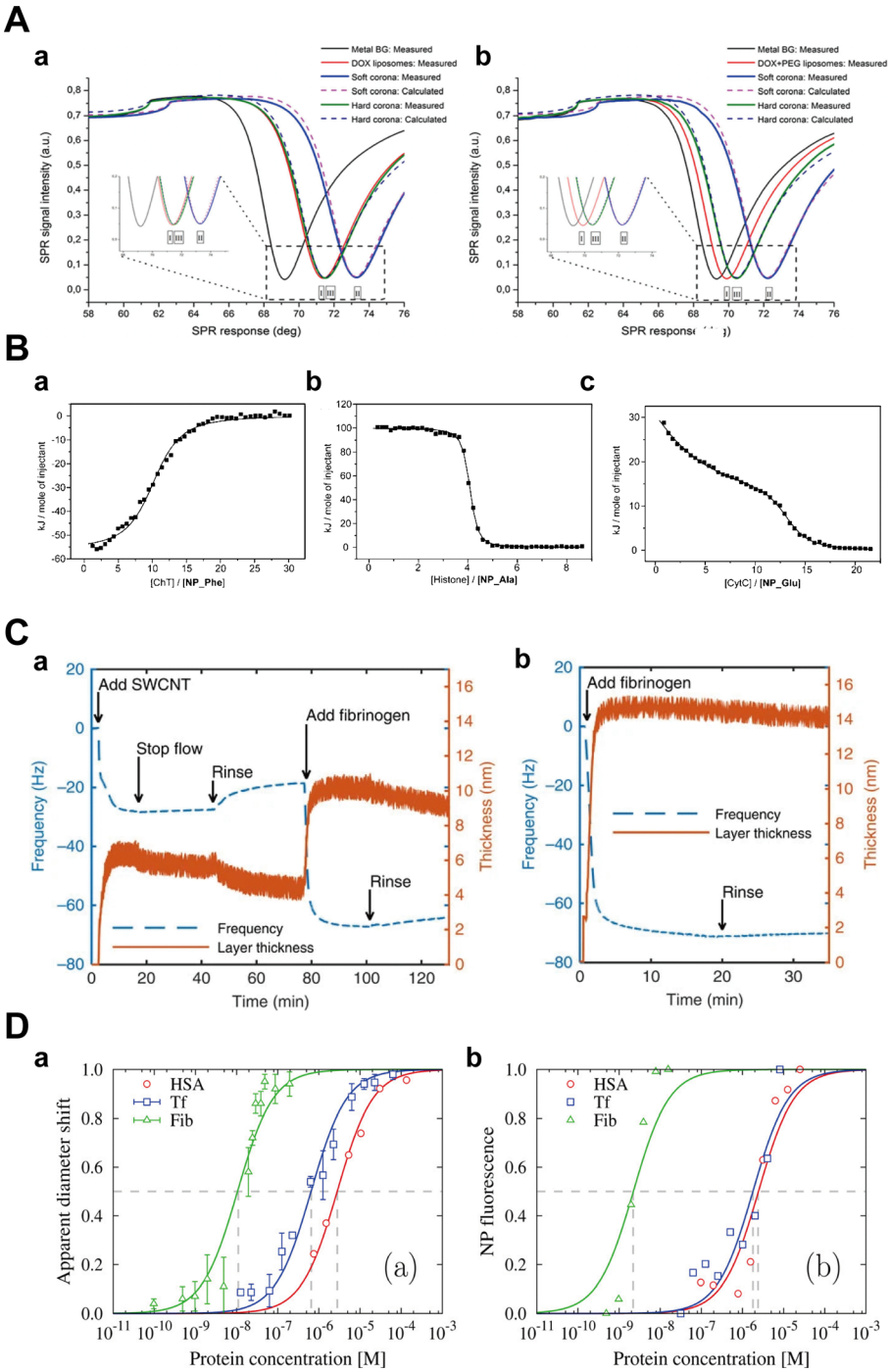

Fig. 10 (A) Interactions between liposomes and proteins; layer modelling for (a) DOX and (b) DOX + PEG liposomes under different conditions using measured full SPR angular spectra. Solid curves and dotted curves represent measured and fitted full SPR spectra, respectively. The black line is SPR spectra of metal sensor surface. I, II, and III represent SPR spectra of pure DOX liposomes, SC, and HC, respectively.[31] Reproduced from ref. 31 with permission from Controlled Release Society. (B) The binding capacity of proteins to NPs detected by ITC; ITC analysis for the binding of (a) ChT with NP_Phe, (b) histone with NP_Ala, and (c) CytC with NP_Glu in 5 mM sodium phosphate buffer (pH = 7.4). The squares represent the integrated heat changes during the formation of the NP–protein complex and the curve fit to the binding isothermal functions.[32] Reproduced from ref. 32 with the permission from American Chemical Society. (C) Changes of frequency (dashed blue curve) and layer thickness (solid orange curve) for a fibrinogen layer deposited on top of a (a) DPPE-PEG5k -SWCNT layer and (b) the gold-coated quartz crystal as measured by QCM-D, and calculated by Voigt viscoelastic model, respectively.[33] Reproduced from ref. 33 with permission from Nature Publishing Group. (D) Characterization of NPs in mono-component protein solutions as a function of protein molar concentration along binding isotherms; (a) normalized apparent diameter of NP–protein complexes to the value of bare NPs; (b) normalized NP fluorescence F_{norm} after NPs diffusion under a thermal gradient. The symbols represent experimental data and the lines are the best fits with related equations.[34] Reproduced from ref. 34 with permission from American Chemical Society.

ions can affect mass change during protein adsorption. Distinguishing the experimental impact of solvents and adsorbed proteins on QCM frequency is particularly challenging.[165] Furthermore, the mass change detected by QCM-D is influenced by the viscoelastic properties of adsorbed proteins, complicating the interpretation of quantitative analysis.

3.3.4 MST. MST, a powerful biophysical technique, detects and quantifies binding events based on the directional motion of fluorescently labelled molecules (such as proteins) under a temperature gradient.[166] By integrating fluorescence detection with thermophoresis, MST offers a sensitive and precise platform for identifying binding-induced interactions between NPs and fluorescently labelled proteins. The normalized relative fluorescence (F_{norm}) and dissociation constant (k_d) can be obtained from the following eqn 7–9.[167]

$$F_{norm} = \frac{F_{hot}}{F_{cold}} \tag{7}$$

$$F_{norm} = (1 - FB)\cdot F_{norm,unbound} + F_{norm,bound} \tag{8}$$

$$FB = \frac{[A] + [B] + k_d - \sqrt{([A] + [B] + k_d)^2 - 4\cdot[AB]}}{2\cdot[B]} \tag{9}$$

F_{hot} is the fluorescence intensity after thermodiffusion and F_{cold} is the initial fluorescence intensity of NPs. $F_{unbound}$ and F_{bound} are the normalized fluorescence intensity of unbound and bound fluorescent proteins, respectively. FB is the bound fraction of [B] while [AB] is the concentration of the binding complexes of [A] and [B]. [A] and [B] are the concentrations of ligands and receptors, respectively.

MST avoids the immobilization procedures necessary for SPR and QCM-D, and minimizes sample consumption compared to ITC, thereby enhancing assay design flexibility.[166] Vilanova *et al.*[34] employed MST and differential centrifugal sedimentation (DCS) to assess the binding affinity of HSA, Tf, and Fib with silica NPs. By analyzing the F_{norm} under thermal gradients, they calculated the k_d order as: HSA > Tf ≫ Fib, corroborated by DCS results (Fig. 10D). Likewise, Wang *et al.*[168] used MST to investigate the binding between BSA and various nanoscale metal–organic frameworks (NMOFs), and they discovered that BSA exhibited a lower binding affinity with amino-modified NMOFs compared to unmodified ones. Despite its high sensitivity to diverse binding-induced interactions, MST cannot measure binding constants in cases of substantial NP aggregation and significant adsorption on the capillaries.[167] Moreover, fluorescence labelling of proteins required in MST may change the protein structure and hence influence the adsorption of protein to NPs.

3.3.5 FRET. FRET relies on the measurement of non-radiative transmission of excitation energy from a donor fluorophore to an acceptor chromophore through dipole–dipole interactions.[146] It has been widespread applied in various biological and biophysical fields, including the investigation of biomolecule-NP binding and protein conformational analysis due to its rapid detection and high sensitivity to the donor–acceptor distance.[147,169,170] The binding parameters of NPs with proteins can be analyzed by fitting the obtained fluorescence data using eqn 10–12:[171]

$$J = \frac{\int_0^\infty F_D\cdot(\lambda)\cdot\varepsilon(\lambda)\cdot\lambda^4 d\lambda}{\int_0^\infty F_D\cdot(\lambda)d\lambda} \tag{10}$$

$$R^6 = 9000\cdot\frac{\ln(10)}{128}\cdot\frac{k^2\cdot\Phi_D}{\pi^5\cdot N_{AV}\cdot n^4} \tag{11}$$

$$E = 1 - \frac{F}{F_0} = \frac{R^6}{R^6 + r^6} = \frac{E_{max}}{1 + \left(\frac{K_D}{C}\right)^n} \tag{12}$$

where J represents the overlap of the fluorescence emission spectrum of the donor and the absorption spectrum of the acceptor, while F_D is the fluorescence spectrum of the donor in the absence of the acceptor. ε and λ are the extinction coefficient and wavelength of the acceptor, respectively. Besides, κ^2 represents the spatial orientation factor, and Φ_D is the quantum yield of the donor. n and N_{AV} represent the refraction coefficient and Avogadro's number, respectively. E denotes the energy transfer efficiency, and E_{max} is the saturation value of FRET efficiency. F and F_0 represent the fluorescence intensities in the presence and absence of proteins, respectively. R is the critical distance between donor and receptor, at which distance the FRET efficiency is 50%. Additionally, r represents the distance between the donor and receptor, and K_D is the dissociation constant. The parameter n in eqn 12 refers to the Hill coefficient, a parameter that describes the degree of interaction between proteins and NPs. C is the concentration of proteins or NPs.

Using FRET, Qu *et al.*[35] investigated HSA adsorption on InP@ZnS quantum dots (QDs) with different chirality (*d*- and *l*-penicillamine), revealing distinct binding behaviors, including the affinity and adsorption orientation related to chirality (Fig. 11A). The K_D value of l-PA-QDs (0.14×10^{-6} m) was approximately 1.65 times lower than that of d-PA-QDs (0.23×10^{-6} m), indicating that the chirality of surface ligands influenced protein binding to QDs. The l-PA-QDs demonstrated a stronger binding affinity compared to d-PA-QDs. Furthermore, the E_{max} value for l-PA-QDs (0.70) was lower than that for d-PA-QDs (0.82), suggesting that HSA may adopt a more compact configuration on the surface of d-PA-QDs compared to l-PA-QDs. These results underscore the potential of FRET in elucidating NP–protein interactions. Nevertheless, the effectiveness of FRET highly relies on the distance between the donor and acceptor, making it challenging to detect loosely bound SC proteins on the outer layers of NPs. Moreover, while FRET analysis detects NP–protein interactions, it does not yield quantitative and qualitative insights into the protein corona, *e.g.*, adsorption amount and corona compositions.

3.3.6 New characterization methods. New characterization methods have been developed to overcome the challenges in protein corona formation detection. To distinguish the ''hard'' from the ''soft'' corona, Weiss *et al.*[172] monitored the real-time evolution of protein corona formation on silica NPs using confocal laser scanning microscopy (CLSM) combined with

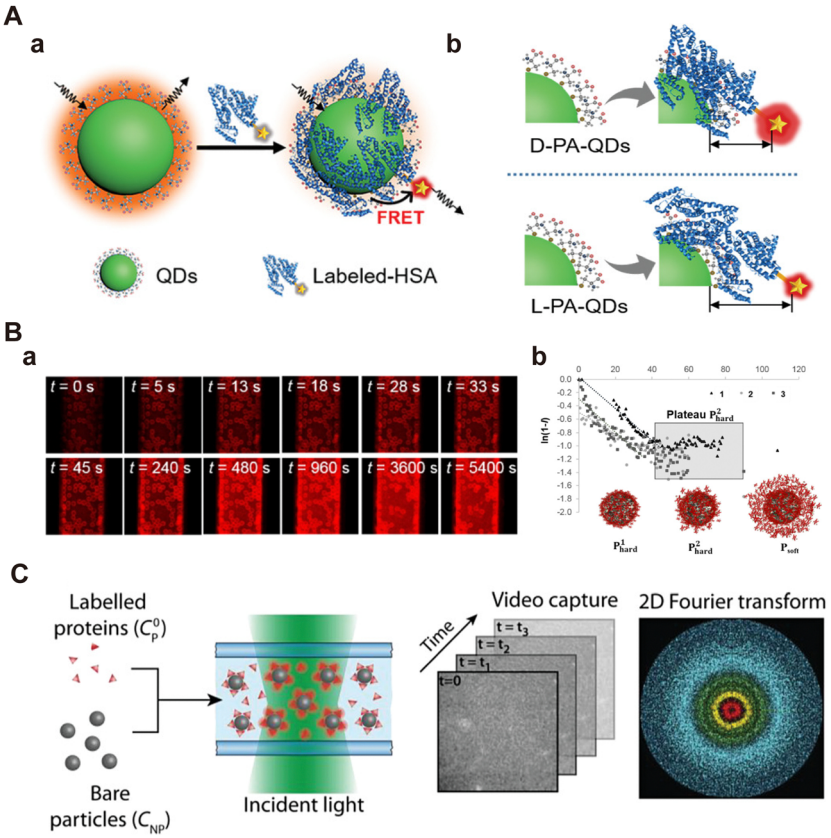

Fig. 11 (A) (a) Schematic representation of FRET between InP@ZnS QDs and fluorescently labeled HAS; (b) schematics of the FRET of chiral InP@ZnS QDs.[35] Reproduced from ref. 35 with the permission from Wiley-VCH. (B) Kinetics of protein corona formation around silica particles under static particle conditions; (a) representative images obtained from 2D CLSM imaging, depicting the changes in fluorescence intensity of NPs during incubation; (b) an enlarged version of linearized data, focusing mainly on the first two phases of adsorption.[172] Reproduced from ref. 172 with permission from American Chemical Society. (C) Standard workflow of DDM: bare NPs are mixed with labeled proteins followed by transferring the mixture into a glass capillary for fluorescence microscopy imaging. Time series of images are then analyzed to extract the 2D Fourier transform and the differential image correlation function (DICF).[173] Reproduced from ref. 173 with permission from Wiley-VCH.

microfluidics (MF). By immobilizing silica NPs in the MF channel and injecting fluorescently labeled HSA, precise quantification of surface fluorescence intensity of NPs can be achieved through CLSM with meticulous regulation of key parameters like channel size and flow rate. The results revealed three distinct phases in the protein corona formation process: phase 1 (P^1_{hard}) representing the high-affinity protein adsorption and formation of HC, phase 2 (P^2_{hard}) signifying irreversible HC protein interaction with newly adsorbed proteins, and phase 3 (P^3_{soft}) representing the final reversible SC formation (Fig. 11B). While this technique shows promise in defining new cutting-edge protocols for studying protein corona kinetics and differentiating protein layers, it encountered challenges in distinguishing fluorescent signals between proteins adhered to NPs and those attached to the immobilized channel. Moreover, the intricate control of parameters in the MF setup may increase application complexity and experimental errors.

Latreille *et al.*[173] applied differential dynamic microscopy (DDM) in fluorescence imaging mode to quantitatively assess protein adsorption on NPs and monitor the resulting NP aggregation behaviors *in situ*. Their experimental setup involved a standard epifluorescence microscope equipped with an sCMOS camera. Upon the adsorption of fluorescently labeled proteins onto the surface of polystyrene NPs, the NP surface emitted fluorescence signals. By analyzing the fluorescence fluctuations resulting from NP Brownian diffusion, DDM quantifies the contributions of free and adsorbed proteins in NP–protein interactions (Fig. 11C). The results showed that protein adsorption promoted the NP aggregation over a wide concentration range. Moreover, the binding affinity of proteins to polystyrene NPs was dependent on NP concentration, and the composition of protein corona changed with the dilution of proteins in complex solutions. This method is primarily suitable for isotropic NPs (spherical NPs) and may require adjustments when applied to highly anisotropic NPs such as nanorods, nanocubes, and nanosheets.

3.4 Characterization of the conformation change of proteins

Protein binding to NPs can induce significant conformational or structural changes of adsorbed proteins. Given the biological significance of such structural alterations in maintaining physiological homeostasis, it is essential to investigate the impact

of NP–protein interactions on protein structure.[174–176] Commonly used characterization techniques include circular dichroism (CD) spectroscopy, surface-enhanced Raman scattering (SERS), and nuclear magnetic resonance spectroscopy (NMR).

3.4.1 CD. The far ultraviolet (UV) region (190–250 nm) of CD spectroscopy is commonly utilized for monitoring protein peptide bonds, facilitating the determination of alterations in the secondary structure of proteins bound to NPs, including variations in α-helix, β-sheet, β-turn, and random coil conformations.[177,178] Liu *et al.*[36] analyzed the conformation changes of fibrinogen (Fg) proteins upon adsorption to particulate matter (PM2.5). The results revealed a decrease in the α-helix rate from 16% to 6%, accompanied by an increase in the β-sheet content from 31% to 39% in the presence of PM2.5 (Fig. 12A), indicating that the interaction with PM2.5 led to alterations in the secondary structure of Fg. Similarly, CD spectroscopy was utilized to investigate the impact of SWCNT

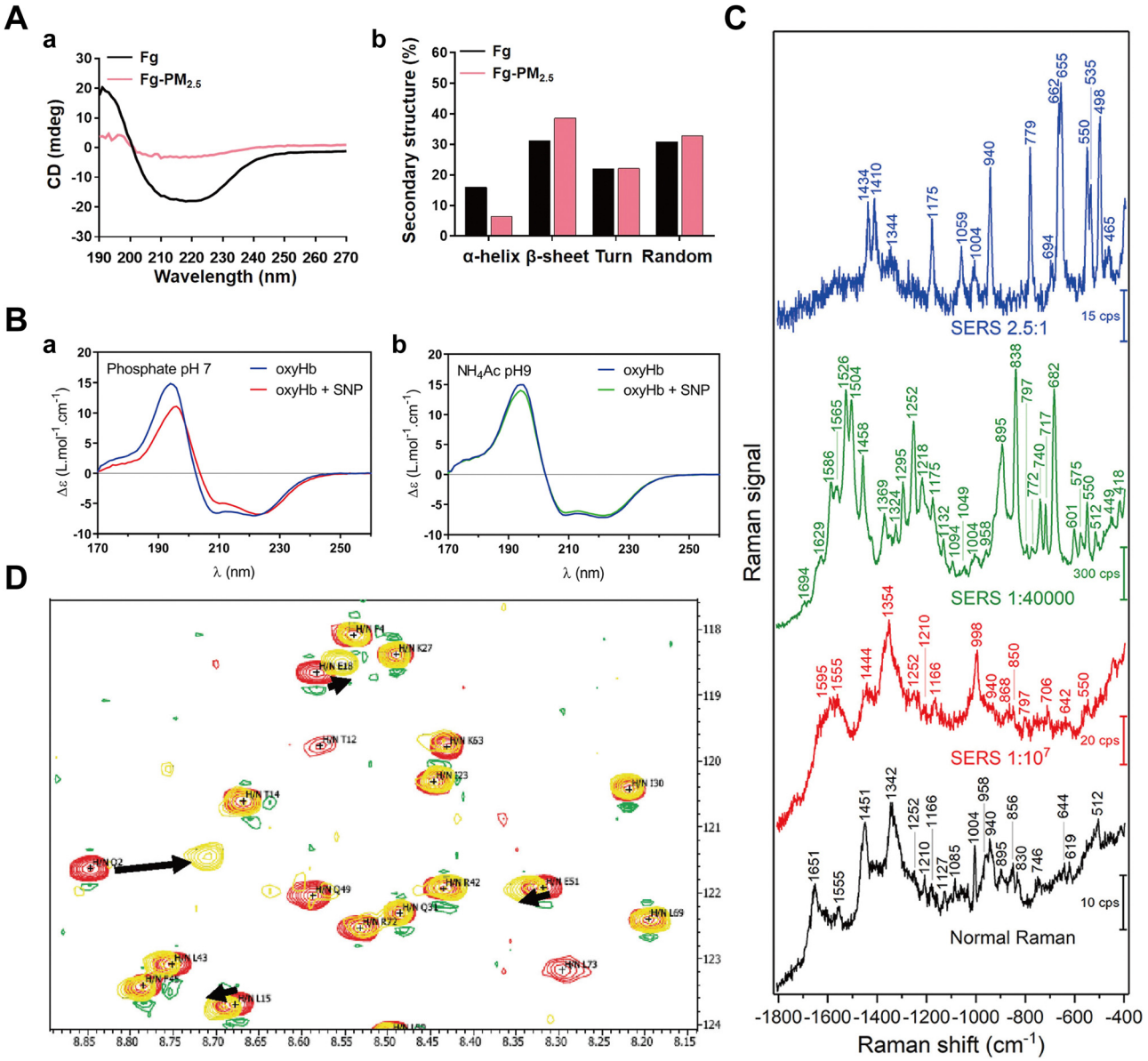

Fig. 12 (A) Secondary structure changes detected by CD; (a) CD spectra of Fg in the absence and presence of PM2.5; (b) Content of α-helix, β-sheet, turn and random of Fg in the absence and presence of PM2.5, calculated by DichroWeb.[36] Reproduced from ref. 36 with permission from Elsevier Ltd. (B) SRCD spectroscopy of oxyHb in the absence and presence of SNPs at 22 °C in (a) phosphate buffer pH 7 and (b) NH_4Ac buffer pH 9.[180] Reproduced from ref. 180 with permission from American Chemical Society. (C) SERS spectroscopy of BSA solution in the absence and presence of Au NPs. The blank curve is the SERS spectroscopy of pure BSA. The red, green, and blue curves represent the SERS spectroscopy of the sample with the Au NPs : BSA ratio of $1:10^7$, 1 : 140 000, and 2.5 : 1, respectively.[37] Reproduced from ref. 37 with permission from Frontiers. (D) 2D [^{15}N-^{1}H] NMR spectroscopy of free hUbq (red) and hUbq plus Au NP (yellow) samples at pH 7. Black arrows indicate NH backbone groups with the largest chemical shift perturbations (Q2, L15, and E18) in this spectral window.[181] Reproduced from ref. 38 with permission from American Chemical Society.

incubation on the conformation change of BFG, gamma globulin (Ig), Tf, and BSA.[179] Significant conformational changes in BFG and Ig were observed after a 10-min incubation with SWCNTs, and these alterations remained largely unchanged over extended incubation periods. Although CD spectroscopy provides information about structural changes in proteins, it requires a high concentration of protein samples and cannot provide detailed information on the conformation of target proteins in complex environments due to interference from other proteins or cells.

Synchrotron-radiation circular dichroism (SRCD) is exploited as an advanced tool for characterizing protein structures.[182] Leveraging the intense light of a synchrotron beam, SRCD improves the precision of CD spectroscopy and facilitates the analysis of protein structures in the low UV regions.[183] Sanchez-Guzman *et al.*[180] applied SRCD to investigate the impact of silica NPs on the secondary structure of oxyhemoglobin (oxyHb) present in SC and HC, revealing significant alterations in the secondary structure of oxyHb within the HC, while no influence on the weakly bound oxyHb in the SC (Fig. 12B). Notably, light scattering arising from aggregated or large particles can potentially interfere with CD results.

3.4.2 SERS. When proteins adsorb onto or come into proximity with the active surface of SERS (mainly metal NPs like Ag or AuNPs), they generate enhanced Raman scattering signals that provide insights into protein conformation and side-chain environments based on their vibrational characteristics.[184–186] Using SERS spectroscopy, Szekeres *et al.*[37] examined the structural changes of BSA upon exposure to Au NPs, revealing alterations in BSA conformation upon the BSA–NP interaction (Fig. 12C). Similarly, Kuschnerus *et al.*[187] examined structural changes of BSA exposed to mesoporous silica particles (MSPs) using SERS, indicating significant conformational changes in adsorbed BSA on NPs. However, SERS is limited to metal NPs and is not applicable to materials like carbon, silica, or polymers. The weak Raman signal necessitates highly sensitive instrumentation with optimized parameters, and sample fluorescence can interfere with detection. Additionally, SERS does not provide information on the composition of protein corona.

3.4.3 NMR spectroscopy. Diffusion ordered NMR spectroscopy (DOSY-NMR) has been used for quantifying the size changes of NPs in dispersions resulting from NP–protein interactions.[188] DOSY-NMR correlates the changes in the NMR signals of specific atoms/groups (such as ^{19}F) within NPs to their Brownian motion, thereby offering an effective method to measure the diffusion coefficient of various materials.[189] In addition to detecting size changes, NMR is predominantly employed for investigating structural modification of proteins induced by their interactions with NPs. Leveraging the magnetic properties of ^{1}H, ^{13}C, ^{15}N, ^{19}F, ^{29}Si, and ^{31}P nuclei, NMR spectroscopy enables the analysis of chemical shifts, intensity, and linewidth of analytes.[190] Owing to the unique chemical shifts and intensity of specific NPs and proteins, alterations in chemical shifts and intensity in conventional NMR spectra can accurately reflect the impact of NP–protein interactions on protein structures.[191] Lundqvist *et al.*[192] investigated the effect of silica NPs with varying diameters on the secondary structure of human carbonic anhydrase I (HCAI) by NMR spectroscopy. Their findings revealed that the curvature of silica NPs strongly affected the secondary structure of HCAI, with larger perturbations observed with silica NPs displaying larger diameters. Additionally, the results indicated that the tertiary structures of HCAI were unaffected by the curvatures of the silica NPs. Calzola *et al.*[181] employed NMR spectroscopy to analyze the interactions between ubiquitin protein and Au NPs, and the 2D [$^{15}N-^{1}H$] NMR spectra showed that the presence of Au NPs affected the position of specific peaks, indicating the interaction of a specific domain of human ubiquitin with Au NPs (Fig. 12D). NMR faces challenges due to

Table 3 Characterization methods for investigating protein corona on NPs

Characteristics	Characterization methods	Abbreviations	Brief description	Ref.
Size changes	Dynamic light scattering	DLS	Hydrodynamic size	102 and 104
	Nanoparticle tracking analysis	NTA	NP concentration and size	108 and 110
	Fluorescence correlation spectroscopy	FCS	Changes in diffusion coefficient and size of NP	26 and 117
	Diffusion ^{19}fluorine-magnetic resonance	^{19}F-NMR	Changes in diffusion coefficient and size of NP	120
Change of morphology	Transmission electron microscopy	TEM	Morphology of NP–protein complex	128
	Cryogenic TEM	Cryo-TEM		28
	Scanning electron microscopy	SEM	Thickness of protein corona	132
	Atomic force microscopy	AFM		134
NP–protein interactions	Surface plasmon resonance	SPR	Adsorption kinetic parameters	138
	Isothermal titration calorimetry	ITC	Thermodynamic parameters of binding	140 and 141
	Quartz crystal microbalance with dissipation monitoring	QCM-D	Mass changes induced by protein adsorption	144
	Microscale thermophoresis	MST	Non-radiative transmission of excitation energy	145
	Fluorescence resonance energy transfer	FRET	Binding parameters	147
Conformation changes of protein	Circular dichroism	CD	Secondary structural changes of proteins induced by NP–protein interaction	177
	Surface-enhanced Raman scattering	SERS		184
	Nuclear magnetic resonance	NMR		190

complex sample preparation and a time-consuming, costly measurement process. Additionally, its weak signals make it unsuitable for analyzing sulfur-containing structures. Compared to other methods for structural analysis, the high molecular weight of proteins and the difficulty of interpreting NMR spectra in the presence of free proteins within complex fluids further limit NMR's application in protein corona studies.[38]

The above-mentioned methods for protein corona characterization are summarized in Table 3.

4. Conclusions and outlook

The coverage of blood proteins reshapes the innate surface properties of NPs and thus dictates their ultimate fate *in vivo*, impacting critical behaviors such as pharmacokinetics, biodistribution, targetability, and therapeutic efficacy. A comprehensive understanding of NP–protein interaction along with an insight into the composition of protein corona is crucial for elucidating the suboptimal therapeutic outcomes of nanomedicines during clinical trials and advancing the clinical translation of nanomedicines. This review provides an overview of separation and *in situ* characterization techniques for comprehensively unravelling the intricacies inherent in NP–protein interactions.

Previous techniques for characterizing the protein corona *in situ* are primarily focused on the size, morphology, and adsorption kinetics, yet lack robust tools for quantification of the protein corona. Although the BCA assay offers a means to quantify corona proteins, the process of detaching adsorbed proteins from NPs following the isolation of NP–protein complexes from the incubation medium may lead to the loss and alteration of protein corona fingerprints.[193,194] Consequently, current research has focused on developing new methods that allow *in situ* quantitative analysis of protein corona. Lo Giudice *et al.*[195] utilized flow cytometry to investigate NP–protein interactions by employing an immunoprobe (mTfQD630) designed to specifically recognize the Tf epitope AA. This approach facilitated the *in situ* characterization of specific motifs presenting in the biomolecular corona, thereby contributing to a better understanding and potential prediction of NP-biomolecular interactions with cells. Moreover, a key focus in current protein corona analysis lies in achieving direct and quantitative determination of NP–protein interactions *in situ* and at the single-NP level. For instance, Tan *et al.*[196] developed an innovative real-time three-dimensional single-particle-tracking microscopy combined with a lock-on filtering algorithm (RTY-3D-SPT) to detect the NPs-protein interactions at the single particle level, providing insights into *in situ* protein corona on a per-particle basis and bridging gaps in corona characterization at the single-particle level. Although significant strides have been made in characterizing the protein corona, the direct deciphering of protein corona compositions *in situ* and understanding the heterogeneity among NPs remain challenging.

Nonspecific NP–protein interactions are typically highly heterogeneous, resulting in an undetectable biological behaviors for individual NPs. Therefore, in addition to detecting the NP–protein interactions *in situ* and at the single-NP level, it is also important to analyze the heterogeneity of protein interaction among different NPs. Niu *et al.*[197] established an *in situ* approach allowing quantitative analysis of NP−blood protein adsorption at the individual NP level and also the interparticle heterogeneity of NP–protein interactions based on a dual fluorescence quantification technique. This approach not only allowed the *in situ* quantitative monitoring of protein adsorption kinetics and the aggregation status of NPs in the serum, it also revealed the interparticle heterogeneity of NP–protein interactions with the single-NP resolution.

In summary, achieving a precise and comprehensive analysis of the protein corona requires careful consideration of several crucial points. Firstly, gaining a holistic understanding of various aspects of the protein corona require the application of multiple complementary techniques, given the distinct focus of these methods. Secondly, standardizing both preparation and characterization procedures is a prerequisite for generating reproducible data, therefore providing reliable insights into the biological effects of nanomedicines. Thirdly, characterizing NPs at the single-particle level is essential to unveil the heterogeneity of NPs and their intricate interactions with proteins, potentially leading to varied behaviors among NPs within the same sample. Last but not least, multi-omics approaches should be applied to obtain insights into proteins as well as lipids and other relevant components present in phycological fluids associated with NPs. Looking forward, collaborative interdisciplinary efforts hold great promise of inspiring breakthroughs in the characterization of protein corona in the future.

Data avaibility

No primary research results, software or code have been included and no new data were generated or analysed as part of this review.

Conflicts of interest

There are no conflicts to declare.

Acknowledgements

This work was financially supported by the National Science Foundation of China (32201149) and the Shandong Provincial Natural Science Fund for Excellent Young Scientists Fund Program (Overseas) (2022HWYQ-063). Open Access funding provided by the Max Planck Society.

References

1 B. Pelaz, C. Alexiou, R. A. Alvarez-Puebla, F. Alves, A. M. Andrews, S. Ashraf, L. P. Balogh, L. Ballerini, A. Bestetti, C. Brendel, S. Bosi, M. Carril, W. C. W. Chan, C. Chen, X. Chen, X. Chen, Z. Cheng, D. Cui, J. Du, C. Dullin,

A. Escudero, N. Feliu, M. Gao, M. George, Y. Gogotsi, A. Grünweller, Z. Gu, N. J. Halas, N. Hampp, R. K. Hartmann, M. C. Hersam, P. Hunziker, J. Jian, X. Jiang, P. Jungebluth, P. Kadhiresan, K. Kataoka, A. Khademhosseini, J. Kopeček, N. A. Kotov, H. F. Krug, D. S. Lee, C.-M. Lehr, K. W. Leong, X.-J. Liang, M. Ling Lim, L. M. Liz-Marzán, X. Ma, P. Macchiarini, H. Meng, H. Möhwald, P. Mulvaney, A. E. Nel, S. Nie, P. Nordlander, T. Okano, J. Oliveira, T. H. Park, R. M. Penner, M. Prato, V. Puntes, V. M. Rotello, A. Samarakoon, R. E. Schaak, Y. Shen, S. Sjöqvist, A. G. Skirtach, M. G. Soliman, M. M. Stevens, H.-W. Sung, B. Z. Tang, R. Tietze, B. N. Udugama, J. S. VanEpps, T. Weil, P. S. Weiss, I. Willner, Y. Wu, L. Yang, Z. Yue, Q. Zhang, Q. Zhang, X.-E. Zhang, Y. Zhao, X. Zhou and W. J. Parak, *ACS Nano*, 2017, **11**, 2313–2381.

2 J. Shi, P. W. Kantoff, R. Wooster and O. C. Farokhzad, *Nat. Rev. Cancer*, 2017, **17**, 20–37.

3 M. A. Younis, H. M. Tawfeek, A. A. H. Abdellatif, J. A. Abdel-Aleem and H. Harashima, *Adv. Drug Delivery Rev.*, 2022, **181**, 114083.

4 K. E. Wheeler, A. J. Chetwynd, K. M. Fahy, B. S. Hong, J. A. Tochihuitl, L. A. Foster and I. Lynch, *Nat. Nanotechnol.*, 2021, **16**, 617–629.

5 P. L. Latreille, M. Le Goas, S. Salimi, J. Robert, G. De Crescenzo, D. C. Boffito, V. A. Martinez, P. Hildgen and X. Banquy, *ACS Nano*, 2022, **16**, 1689–1707.

6 S. Abbina, L. E. Takeuchi, P. Anilkumar, K. Yu, J. C. Rogalski, R. A. Shenoi, I. Constantinescu and J. N. Kizhakkedathu, *Nat. Commun.*, 2020, **11**, 3048.

7 M. Safi, J. Courtois, M. Seigneuret, H. Conjeaud and J. F. Berret, *Biomaterials*, 2011, **32**, 9353–9363.

8 F. Barbero, S. Michelini, O. H. Moriones, J. Patarroyo, J. Rosell, M. F. Gusta, M. Vitali, L. Martín, F. Canals, A. Duschl, J. Horejs-Hoeck, L. Mondragón, N. G. Bastús and V. Puntes, *Bioconjugate Chem.*, 2022, **33**, 1505–1514.

9 V. P. Vu, G. B. Gifford, F. Chen, H. Benasutti, G. Wang, E. V. Groman, R. Scheinman, L. Saba, S. M. Moghimi and D. Simberg, *Nat. Nanotechnol.*, 2019, **14**, 260–268.

10 F. Chen, G. Wang, J. I. Griffin, B. Brenneman, N. K. Banda, V. M. Holers, D. S. Backos, L. Wu, S. M. Moghimi and D. Simberg, *Nat. Nanotechnol.*, 2017, **12**, 387–393.

11 N. Bertrand, P. Grenier, M. Mahmoudi, E. M. Lima, E. A. Appel, F. Dormont, J.-M. Lim, R. Karnik, R. Langer and O. C. Farokhzad, *Nat. Commun.*, 2017, **8**, 777.

12 F. Barbero, L. Russo, M. Vitali, J. Piella, I. Salvo, M. L. Borrajo, M. Busquets-Fité, R. Grandori, N. G. Bastús, E. Casals and V. Puntes, *Semin. Immunol.*, 2017, **34**, 52–60.

13 L. Digiacomo, D. Pozzi, S. Palchetti, A. Zingoni and G. Caracciolo, *Wiley Interdiscip. Rev.: Nanomed. Nanobiotechnol.*, 2020, **12**, e1615.

14 M. Tonigold, J. Simon, D. Estupiñán, M. Kokkinopoulou, J. Reinholz, U. Kintzel, A. Kaltbeitzel, P. Renz, M. P. Domogalla, K. Steinbrink, I. Lieberwirth, D. Crespy, K. Landfester and V. Mailänder, *Nat. Nanotechnol.*, 2018, **13**, 862–869.

15 S. Schöttler, G. Becker, S. Winzen, T. Steinbach, K. Mohr, K. Landfester, V. Mailänder and F. R. Wurm, *Nat. Nanotechnol.*, 2016, **11**, 372–377.

16 M. Li, S. Jiang, J. Simon, D. Paßlick, M.-L. Frey, M. Wagner, V. Mailänder, D. Crespy and K. Landfester, *Nano Lett.*, 2021, **21**, 1591–1598.

17 S. Jiang, D. Prozeller, J. Pereira, J. Simon, S. Han, S. Wirsching, M. Fichter, M. Mottola, I. Lieberwirth, S. Morsbach, V. Mailänder, S. Gehring, D. Crespy and K. Landfester, *Nanoscale*, 2020, **12**, 2626–2637.

18 G. Perini, F. Giulimondi, V. Palmieri, A. Augello, L. Digiacomo, E. Quagliarini, D. Pozzi, M. Papi and G. Caracciolo, *Pharmaceutics*, 2021, **13**, 378.

19 P. C. Ke, S. Lin, W. J. Parak, T. P. Davis and F. Caruso, *ACS Nano*, 2017, **11**, 11773–11776.

20 C. Weber, S. Morsbach and K. Landfester, *Angew. Chem., Int. Ed.*, 2019, **58**, 12787–12794.

21 S. Winzen, S. Schoettler, G. Baier, C. Rosenauer, V. Mailaender, K. Landfester and K. Mohr, *Nanoscale*, 2015, **7**, 2992–3001.

22 S. Milani, F. Baldelli Bombelli, A. S. Pitek, K. A. Dawson and J. Rädler, *ACS Nano*, 2012, **6**, 2532–2541.

23 T. Cedervall, I. Lynch, M. Foy, T. Berggård, S. C. Donnelly, G. Cagney, S. Linse and K. A. Dawson, *Angew. Chem., Int. Ed.*, 2007, **46**, 5754–5756.

24 C. Wang, B. Chen, M. He and B. Hu, *ACS Nano*, 2021, **15**, 3108–3122.

25 K. Kristensen, R. Münter, P. J. Kempen, M. E. Thomsen, A. Stensballe and T. L. Andresen, *Acta Biomater.*, 2021, **130**, 460–472.

26 L. Shang and G. U. Nienhaus, *Acc. Chem. Res.*, 2017, **50**, 387–395.

27 M. Kokkinopoulou, J. Simon, K. Landfester, V. Mailänder and I. Lieberwirth, *Nanoscale*, 2017, **9**, 8858–8870.

28 S. Sheibani, K. Basu, A. Farnudi, A. Ashkarran, M. Ichikawa, J. F. Presley, K. H. Bui, M. R. Ejtehadi, H. Vali and M. Mahmoudi, *Nat. Commun.*, 2021, **12**, 1–9.

29 V. Mirshafiee, R. Kim, S. Park, M. Mahmoudi and M. L. Kraft, *Biomaterials*, 2016, **75**, 295–304.

30 Y. Chong, C. Ge, Z. Yang, J. A. Garate, Z. Gu, J. K. Weber, J. Liu and R. Zhou, *ACS Nano*, 2015, **9**, 5713–5724.

31 O. K. Kari, T. Rojalin, S. Salmaso, M. Barattin, H. Jarva, S. Meri, M. Yliperttula, T. Viitala and A. Urtti, *Drug Delivery Transl. Res.*, 2017, **7**, 228–240.

32 M. De, C.-C. You, S. Srivastava and V. M. Rotello, *J. Am. Chem. Soc.*, 2007, **129**, 10747–10753.

33 G. Bisker, J. Dong, H. D. Park, N. M. Iverson, J. Ahn, J. T. Nelson, M. P. Landry, S. Kruss and M. S. Strano, *Nat. Commun.*, 2016, **7**, 10241.

34 O. Vilanova, J. J. Mittag, P. M. Kelly, S. Milani, K. A. Dawson, J. O. Rädler and G. Franzese, *ACS Nano*, 2016, **10**, 10842–10850.

35 S. Qu, F. Sun, Z. Qiao, J. Li and L. Shang, *Small*, 2020, **16**, 1–7.

36 Z. Liu, Q. Zhu, E. Song and Y. Song, *J. Hazard. Mater.*, 2021, **414**, 125499.

37 G. P. Szekeres and J. Kneipp, *Front. Chem.*, 2019, **7**, 30.
38 V. P. Brahmkhatri, A. Singh, A. Chakraborty, R. S. Sharma, K. Chandra and H. S. Atreya, *Appl. Surf. Sci. Adv.*, 2022, **11**, 100272.
39 C. Pisani, J. C. Gaillard, C. Dorandeu, C. Charnay, Y. Guari, J. Chopineau, J. M. Devoisselle, J. Armengaud and O. Prat, *Nanoscale*, 2017, **9**, 5769–5772.
40 L. Digiacomo, F. Giulimondi, A. L. Capriotti, S. Piovesana, C. M. Montone, R. Z. Chiozzi, A. Laganà, M. Mahmoudi, D. Pozzi and G. Caracciolo, *Nanoscale Adv.*, 2021, **3**, 3824–3834.
41 W. W.-F. Leung, *Centrifugal Separations in Biotechnology*, 2007, 19–35.
42 M. Singh, H. Chand and K. C. Gupta, *Chem. Biodiversity*, 2005, **2**, 809–824.
43 M. Iqbal and R. E. Verrall, *J. Phys. Chem.*, 1987, **91**, 1935–1941.
44 F. Pederzoli, G. Tosi, M. A. Vandelli, D. Belletti, F. Forni and B. Ruozi, *Wiley Interdiscip. Rev.: Nanomed. Nanobiotechnol.*, 2017, **9**, 1–23.
45 T. Lima, K. Bernfur, M. Vilanova and T. Cedervall, *Sci. Rep.*, 2020, **10**, 1–9.
46 G. Caracciolo, L. Callipo, S. C. De Sanctis, C. Cavaliere, D. Pozzi and A. Laganà, *Biochim. Biophys. Acta, Biomembr.*, 2010, **1798**, 536–543.
47 R. Pattipeiluhu, S. Crielaard, I. Klein-Schiphorst, B. I. Florea, A. Kros and F. Campbell, *ACS Cent. Sci.*, 2020, **6**, 535–545.
48 M. Brückner, J. Simon, S. Jiang, K. Landfester and V. Mailänder, *Acta Biomater.*, 2020, **114**, 333–342.
49 L. Böhmert, L. Voß, V. Stock, A. Braeuning, A. Lampen and H. Sieg, *Nanoscale Adv.*, 2020, **2**, 563–582.
50 T. P. Doan-Nguyen and D. Crespy, *Chem. Soc. Rev.*, 2022, **51**, 8612–8651.
51 D. Docter, U. Distler, W. Storck, J. Kuharev, D. Wünsch, A. Hahlbrock, S. K. Knauer, S. Tenzer and R. H. Stauber, *Nat. Protoc.*, 2014, **9**, 2030–2044.
52 A. Perez-Potti, H. Lopez, B. Pelaz, A. Abdelmonem, M. G. Soliman, I. Schoen, P. M. Kelly, K. A. Dawson, W. J. Parak, Z. Krpetic and M. P. Monopoli, *Sci. Rep.*, 2021, **11**, 6443.
53 D. Di Silvio, N. Rigby, B. Bajka, A. Mayes, A. Mackie and F. Baldelli Bombelli, *Nanoscale*, 2015, **7**, 11980–11990.
54 M. Werwie, N. Fehr, X. Xu, T. Basché and H. Paulsen, *Biochim. Biophys. Acta, Gen. Subj.*, 2014, **1840**, 1651–1656.
55 K. S. Siddiqi, A. Ur Rahman, T. Tajuddin and A. Husen, *Nanoscale Res. Lett.*, 2016, **11**, 498.
56 U. Sakulkhu, M. Mahmoudi, L. Maurizi, G. Coullerez, M. Hofmann-Amtenbrink, M. Vries, M. Motazacker, F. Rezaee and H. Hofmann, *Biomater. Sci.*, 2015, **3**, 265–278.
57 K. N. L. Hoang, K. E. Wheeler and C. J. Murphy, *Anal. Chem.*, 2022, **94**, 4737–4746.
58 D. Bonvin, D. Chiappe, M. Moniatte, H. Hofmann and M. Mionić Ebersold, *Analyst*, 2017, **142**, 3805–3815.
59 J. E. Blume, W. C. Manning, G. Troiano, D. Hornburg, M. Figa, L. Hesterberg, T. L. Platt, X. Zhao, R. A. Cuaresma, P. A. Everley, M. Ko, H. Liou, M. Mahoney, S. Ferdosi, E. M. Elgierari, C. Stolarczyk, B. Tangeysh, H. Xia, R. Benz, A. Siddiqui, S. A. Carr, P. Ma, R. Langer, V. Farias and O. C. Farokhzad, *Nat. Commun.*, 2020, **11**, 1–14.
60 A. A. Ashkarran, N. Dararatana, D. Crespy, G. Caracciolo and M. Mahmoudi, *Nanoscale*, 2020, **12**, 2374–2383.
61 E. Quagliarini, L. Digiacomo, D. Caputo, A. Coppola, H. Amenitsch, G. Caracciolo and D. Pozzi, *Nanomaterials*, 2022, 12.
62 A. J. Chetwynd, E. J. Guggenheim, S. M. Briffa, J. A. Thorn, I. Lynch and E. Valsami-Jones, *Nanomaterials*, 2018, **8**, 99.
63 A. L. Capriotti, G. Caracciolo, C. Cavaliere, V. Colapicchioni, S. Piovesana, D. Pozzi and A. Laganà, *Chromatographia*, 2014, **77**, 755–769.
64 N. Li, S. Zeng, L. He and W. Zhong, *Anal. Chem.*, 2010, **82**, 7460–7466.
65 A. K. Brewer, *Chromatographia*, 2021, **84**, 807–811.
66 A. Oliva, M. Llabrés and J. B. Fariña, *J. Pharm. Biomed. Anal.*, 2001, **25**, 833–841.
67 P. Hong, S. Koza and E. S. P. Bouvier, *J. Liq. Chromatogr. Relat. Technol.*, 2012, **35**, 2923–2950.
68 T.-Y. Huang, L.-M. Chi and K.-Y. Chien, *J. Chromatogr. A*, 2018, **1571**, 201–212.
69 S. Fekete, A. Beck, J.-L. Veuthey and D. Guillarme, *J. Pharm. Biomed. Anal.*, 2014, **101**, 161–173.
70 K. Kristensen, T. B. Engel, A. Stensballe, J. B. Simonsen and T. L. Andresen, *J. Controlled Release*, 2019, **307**, 1–15.
71 M. Hadjidemetriou, Z. Al-Ahmady, M. Mazza, R. F. Collins, K. Dawson and K. Kostarelos, *ACS Nano*, 2015, **9**, 8142–8156.
72 K. Yang, B. Mesquita, P. Horvatovich and A. Salvati, *Acta Biomater.*, 2020, **106**, 314–327.
73 P. Reschiglian, A. Zattoni, B. Roda, E. Michelini and A. Roda, *Trends Biotechnol.*, 2005, **23**, 475–483.
74 F. Quattrini, G. Berrecoso, J. Crecente-Campo and M. J. Alonso, *Drug Delivery Transl. Res.*, 2021, **11**, 373–395.
75 U. B. Kavurt, M. Marioli, W. T. Kok and D. Stamatialis, *J. Chem. Technol. Biotechnol.*, 2015, **90**, 11–18.
76 T. Otte, H. Pasch, T. Macko, R. Brüll, F. J. Stadler, J. Kaschta, F. Becker and M. Buback, *J. Chromatogr. A*, 2011, **1218**, 4257–4267.
77 F. A. Messaud, R. D. Sanderson, J. R. Runyon, T. Otte, H. Pasch and S. K. R. Williams, *Prog. Polym. Sci.*, 2009, **34**, 351–368.
78 M. Wagner, S. Holzschuh, A. Traeger, A. Fahr and U. S. Schubert, *Anal. Chem.*, 2014, **86**, 5201–5210.
79 G. Yohannes, M. Jussila, K. Hartonen and M.-L. Riekkola, *J. Chromatogr. A*, 2011, **1218**, 4104–4116.
80 I. Alberg, S. Kramer, M. Schinnerer, Q. Hu, C. Seidl, C. Leps, N. Drude, D. Möckel, C. Rijcken, T. Lammers, M. Diken, M. Maskos, S. Morsbach, K. Landfester, S. Tenzer, M. Barz and R. Zentel, *Small*, 2020, **16**(18), 1907574.
81 U. Hansen and A. F. Thünemann, *Langmuir*, 2015, **31**, 6842–6852.
82 J. Ashby, S. Pan and W. Zhong, *ACS Appl. Mater. Interfaces*, 2014, **6**, 15412–15419.

83 J. Ashby, S. Schachermeyer, S. Pan and W. Zhong, *Anal. Chem.*, 2013, **85**, 7494–7501.
84 C. Weber, J. Simon, V. Mailänder, S. Morsbach and K. Landfester, *Acta Biomater.*, 2018, **76**, 217–224.
85 J. D. Robertson, L. Rizzello, M. Avila-Olias, J. Gaitzsch, C. Contini, M. S. Magoń, S. A. Renshaw and G. Battaglia, *Sci. Rep.*, 2016, **6**, 27494.
86 H. Mohammad-Beigi, Y. Hayashi, C. M. Zeuthen, H. Eskandari, C. Scavenius, K. Juul-Madsen, T. Vorup-Jensen, J. J. Enghild and D. S. Sutherland, *Nat. Commun.*, 2020, **11**(1), 4535.
87 K. A. Dawson and Y. Yan, *Nat. Nanotechnol.*, 2021, **16**, 229–242.
88 D. Baimanov, J. Wang, J. Zhang, K. Liu, Y. Cong, X. Shi, X. Zhang, Y. Li, X. Li, R. Qiao, Y. Zhao, Y. Zhou, L. Wang and C. Chen, *Nat. Commun.*, 2022, **13**(1), 5389.
89 Y. Chu, W. Tang, Z. Zhang, C. Li, J. Qian, X. Wei, T. Ying, W. Lu and C. Zhan, *Nano Lett.*, 2021, **21**, 2124–2131.
90 H. Wang, Y. Lin, K. Nienhaus and G. U. Nienhaus, *Wiley Interdiscip. Rev.: Nanomed. Nanobiotechnol.*, 2018, **10**, e1500.
91 R. García-álvarez and M. Vallet-Regí, *Nanomaterials*, 2021, **11**(4), 888.
92 D. Baimanov, R. Cai and C. Chen, *Bioconjugate Chem.*, 2019, **30**, 1923–1937.
93 A. Tukova, I. C. Kuschnerus, A. Garcia-Bennett, Y. Wang and A. Rodger, *Nanomaterials*, 2021, 11.
94 H. Wang, K. Nienhaus, L. Shang and G. U. Nienhaus, *Chin. J. Chem.*, 2022, **40**, 2685–2693.
95 M. Martinez-Moro, D. Di Silvio and S. E. Moya, *Biophys. Chem.*, 2019, **253**, 106218.
96 A. Maity, S. K. De and A. Chakraborty, *J. Phys. Chem. B*, 2021, **125**, 2113–2123.
97 J. S. Yoneda and M. B. Cardoso, *Nanomedicine*, 2023, **18**, 709–711.
98 S. Kihara, N. J. van der Heijden, C. K. Seal, J. P. Mata, A. E. Whitten, I. Köper and D. J. McGillivray, *Bioconjugate Chem.*, 2019, **30**, 1067–1076.
99 D. Prozeller, S. Morsbach and K. Landfester, *Nanoscale*, 2019, **11**, 19265–19273.
100 X. Xu and J. Dzubiella, *Colloid Polym. Sci.*, 2020, **298**, 747–759.
101 X. Zhang, H. Shi, R. Zhang, J. Zhang, F. Xu, L. Qiao and S. Yu, *Part. Part. Syst. Charact.*, 2019, **36**, 1800257.
102 S. Dominguez-Medina, S. Chen, J. Blankenburg, P. Swanglap, C. F. Landes and S. Link, *Annu. Rev. Phys. Chem.*, 2016, **67**, 489–514.
103 Z. Li, *Phys. Rev. E: Stat. Phys., Plasmas, Fluids, Relat. Interdiscip. Top.*, 2009, **80**, 61204.
104 E. Casals, T. Pfaller, A. Duschl, G. J. Oostingh and V. Puntes, *ACS Nano*, 2010, **4**, 3623–3632.
105 K. Rausch, A. Reuter, K. Fischer and M. Schmidt, *Biomacromolecules*, 2010, **11**, 2836–2839.
106 S. Balog, L. Rodriguez-Lorenzo, C. A. Monnier, M. Obiols-Rabasa, B. Rothen-Rutishauser, P. Schurtenberger and A. Petri-Fink, *Nanoscale*, 2015, **7**, 5991–5997.
107 T. Zhang, C. Dong and J. Ren, *Anal. Chem.*, 2023, **95**, 2029–2038.
108 K. Nienhaus and G. U. Nienhaus, *Biointerphases*, 2020, **15**, 61201.
109 A. Malloy and B. Carr, *Part. Part. Syst. Charact.*, 2006, **23**, 197–204.
110 H. Saveyn, B. De Baets, O. Thas, P. Hole, J. Smith and P. Van der Meeren, *J. Colloid Interface Sci.*, 2010, **352**, 593–600.
111 Z. Varga, B. Fehér, D. Kitka, A. Wacha, A. Bóta, S. Berényi, V. Pipich and J.-L. Fraikin, *Colloids Surf., B*, 2020, **192**, 111053.
112 V. Filipe and A. Hawe, and C. evaluation of N. T. A. (NTA) by N. for the measurement of nanoparticles and protein aggregates. W. Jiskoot, *Pharm. Res.*, 2010, **27**, 796–810.
113 M. S. Bannon, A. López Ruiz, K. Corrotea Reyes, M. Marquez, Z. Wallizadeh, M. Savarmand, C. A. LaPres, J. Lahann and K. McEnnis, *Part. Part. Syst. Charact.*, 2021, **38**, 2100016.
114 A. Jedlovszky-Hajdú, F. B. Bombelli, M. P. Monopoli, E. Tombácz and K. A. Dawson, *Langmuir*, 2012, **28**, 14983–14991.
115 J. Y. Jeong, H. Joung, G. J. Jang and S. Y. Han, *Bull. Korean Chem. Soc.*, 2023, **44**, 551–557.
116 M. Martinez-moro, D. Di Silvio and S. E. Moya, *Biophys. Chem.*, 2019, **253**, 106218.
117 O. Krichevsky and G. Bonnet, *Rep. Prog. Phys.*, 2002, **65**, 251–297.
118 B. Pelaz, P. Del Pino, P. Maffre, R. Hartmann, M. Gallego, S. Rivera-Fernández, J. M. De La Fuente, G. U. Nienhaus and W. J. Parak, *ACS Nano*, 2015, **9**, 6996–7008.
119 I. Negwer, A. Best, M. Schinnerer, O. Schäfer, L. Capeloa, M. Wagner, M. Schmidt, V. Mailänder, M. Helm, M. Barz, H.-J. Butt and K. Koynov, *Nat. Commun.*, 2018, **9**, 5306.
120 R. Mashiach, L. Avram and A. Bar-Shir, *Nano Lett.*, 2022, **22**, 8519–8525.
121 M. Carril, D. Padro, P. Del Pino, C. Carrillo-Carrion, M. Gallego and W. J. Parak, *Nat. Commun.*, 2017, **8**(1), 1542.
122 D. Maiolo, P. Del Pino, P. Metrangolo, W. J. Parak and F. Baldelli Bombelli, *Nanomedicine*, 2015, **10**, 3231–3247.
123 J. Piella, N. G. Bastús and V. Puntes, *Bioconjugate Chem.*, 2016, **28**, 88–97.
124 H. Wang, L. Shang, P. Maffre, S. Hohmann, F. Kirschhöfer, G. Brenner-Weiß and G. U. Nienhaus, *Small*, 2016, **12**, 5836–5844.
125 H. Yin, R. Chen, P. S. Casey, P. C. Ke, T. P. Davis and C. Chen, *RSC Adv.*, 2015, **5**, 73963–73973.
126 M. P. Monopoli, D. Walczyk, A. Campbell, G. Elia, I. Lynch, F. B. Bombelli and K. A. Dawson, *J. Am. Chem. Soc.*, 2011, **133**, 2525–2534.
127 S. Milani, F. Baldelli Bombelli, A. S. Pitek, K. A. Dawson and J. Rädler, *ACS Nano*, 2012, **6**, 2532–2541.
128 Z. S. Al-Ahmady, M. Hadjidemetriou, J. Gubbins and K. Kostarelos, *J. Controlled Release*, 2018, **276**, 157–167.
129 L. Li, X. Jiang and J. Gao, *Adv. Mater. Interfaces*, 2022, **9**, 1–17.

130 L. S. Franqui, M. A. De Farias, R. V. Portugal, C. A. R. Costa, R. R. Domingues, A. G. Souza Filho, V. R. Coluci, A. F. P. Leme and D. S. T. Martinez, *Mater. Sci. Eng., C*, 2019, **100**, 363–377.
131 M. Ovais, S. K. Nethi, S. Ullah, I. Ahmad, S. Mukherjee and C. Chen, *Nanomedicine*, 2020, **15**, 1037–1061.
132 V. Serpooshan, M. Mahmoudi, M. Zhao, K. Wei, S. Sivanesan, K. Motamedchaboki, A. V. Malkovskiy, A. B. Gladstone, J. E. Cohen, P. C. Yang, J. Rajadas, D. Bernstein, Y. J. Woo and P. Ruiz-Lozano, *Adv. Funct. Mater.*, 2015, **25**, 4379–4389.
133 J. Schaefer, C. Schulze, E. E. J. Marxer, U. F. Schaefer, W. Wohlleben, U. Bakowsky and C.-M. Lehr, *ACS Nano*, 2012, **6**, 4603–4614.
134 K. R. Kim, J. Kim, J. H. Back, J. E. Lee and D. R. Ahn, *ACS Nano*, 2021, **16**, 7331–7343.
135 D. Evanko, *Nat. Methods*, 2012, **9**, 778–779.
136 L. Treuel, K. A. Eslahian, D. Docter, T. Lang, R. Zellner, K. Nienhaus, G. U. Nienhaus, R. H. Stauber and M. Maskos, *Phys. Chem. Chem. Phys.*, 2014, **16**, 15053–15067.
137 A. R. Ferhan, J. A. Jackman, T. N. Sut and N.-J. Cho, *Sensors*, 2018, **18**, 1283.
138 T. Cedervall, I. Lynch, S. Lindman, T. Berggård, E. Thulin, H. Nilsson, K. A. Dawson and S. Linse, *Proc. Natl. Acad. Sci. U. S. A.*, 2007, **104**, 2050–2055.
139 M. Reynolds, M. Marradi, A. Imberty, S. Penadés and S. Pérez, *Chem. – Eur. J.*, 2012, **18**, 4264–4273.
140 F. Fu, Z. Huang, W. Wang, W. Wang, X. Ma, L. Wang, Y. Huang, P. Hu, X. Pan and C. Wu, *J. Drug Delivery Sci. Technol.*, 2021, 64.
141 K. Henzler, B. Haupt, K. Lauterbach, A. Wittemann, O. Borisov and M. Ballauff, *J. Am. Chem. Soc.*, 2010, **132**, 3159–3163.
142 S. Lindman, I. Lynch, E. Thulin, H. Nilsson, K. A. Dawson and S. Linse, *Nano Lett.*, 2007, **7**, 914–920.
143 E. H. Pilkington, O. J. R. Gustafsson, Y. Xing, J. Hernandez-Fernaud, C. Zampronio, A. Kakinen, A. Faridi, F. Ding, P. Wilson, P. C. Ke and T. P. Davis, *ACS Nano*, 2018, **12**, 6066–6078.
144 Y. Wang, Y. Sun, M. Li, L. Xiong, X. Xu, N. Ji, L. Dai and Q. Sun, *Food Hydrocolloids*, 2020, **102**, 105615.
145 S. Lippok, S. A. I. Seidel, S. Duhr, K. Uhland, H.-P. Holthoff, D. Jenne and D. Braun, *Anal. Chem.*, 2012, **84**, 3523–3530.
146 J. R. Lakowicz, *Principles of Fluorescence Spectroscopy*, 1983.
147 Y. Feng, L. Liu, S. Hu, P. Zou, J. Zhang, C. Huang, Y. Wang, S. Wang and X. Zhang, *Luminescence*, 2016, **31**, 356–363.
148 B. Douzi, Protein–Protein Interactions: Surface Plasmon Resonance BT - Bacterial Protein Secretion Systems, *Methods and Protocols*, 2017, 257–275.
149 S. G. Patching, *Biochim. Biophys. Acta, Biomembr.*, 2014, **1838**, 43–55.
150 P. G. Stockley and B. Persson, Surface Plasmon Resonance Assays of DNA-Protein Interactions BT - DNA-Protein Interactions, *Principles and Protocols*, 2009, 653–669.
151 A. Patra, T. Ding, G. Engudar, Y. Wang, M. M. Dykas, B. Liedberg, J. C. Y. Kah, T. Venkatesan and C. L. Drum, *Small*, 2016, **12**, 1174–1182.
152 T. Miclăuș, V. E. Bochenkov, R. Ogaki, K. A. Howard and D. S. Sutherland, *Nano Lett.*, 2014, **14**, 2086–2093.
153 M. Zakłos-Szyda, G. Budryn, J. Grzelczyk, H. Pérez-Sánchez and D. Żyżelewicz, *Molecules*, 2020, **25**(1), 206.
154 M. M. Islam, S. Barik and M. Sarkar, *J. Phys. Chem. B*, 2019, **123**, 1512–1526.
155 R. Huang and B. L. T. Lau, *Biochim. Biophys. Acta, Gen. Subj.*, 2016, **1860**, 945–956.
156 J. Tellinghuisen and J. D. Chodera, *Anal. Biochem.*, 2011, **414**, 297–299.
157 A. A. Rehman, H. Ahsan and F. H. Khan, *Int. J. Biol. Macromol.*, 2016, **83**, 366–375.
158 Y. Yu, Y. Luan and W. Dai, *Int. J. Biol. Macromol.*, 2022, **205**, 731–739.
159 M.-M. Yin, W.-Q. Chen, Y.-Q. Lu, J.-Y. Han, Y. Liu and F.-L. Jiang, *Nanoscale*, 2020, **12**, 4573–4585.
160 V. Forest and J. Pourchez, *Nano Today*, 2016, **11**, 700–703.
161 X. Sha, C. Sun, X. Xu, L. Alexander, P. J. Loll and L. S. Penn, *Anal. Chem.*, 2012, **84**, 10298–10305.
162 P. Hampitak, D. Melendrez, M. Iliut, M. Fresquet, N. Parsons, B. Spencer, T. A. Jowitt and A. Vijayaraghavan, *Carbon*, 2020, **165**, 317–327.
163 E. D. Kaufman, J. Belyea, M. C. Johnson, Z. M. Nicholson, J. L. Ricks, P. K. Shah, M. Bayless, T. Pettersson, Z. Feldotö, E. Blomberg, P. Claesson and S. Franzen, *Langmuir*, 2007, **23**, 6053–6062.
164 M. Gagliardi, L. Colagiorgio and M. Cecchini, *Biosensors*, 2023, **13**(6), 607.
165 M. A. Plunkett, P. M. Claesson, M. Ernstsson and M. W. Rutland, *Langmuir*, 2003, **19**, 4673–4681.
166 S. A. I. Seidel, P. M. Dijkman, W. A. Lea, G. van den Bogaart, M. Jerabek-Willemsen, A. Lazic, J. S. Joseph, P. Srinivasan, P. Baaske, A. Simeonov, I. Katritch, F. A. Melo, J. E. Ladbury, G. Schreiber, A. Watts, D. Braun and S. Duhr, *Methods*, 2013, **59**, 301–315.
167 G. Wang, W. Wang, E. Shangguan, S. Gao and Y. Liu, *Mater. Sci. Eng., C*, 2020, **111**, 110830.
168 W. Wang, H. Liu, Z. Huang, F. Fu, W. Wang, L. Wu, Y. Huang, C. Wu and X. Pan, *Chin. Chem. Lett.*, 2022, **33**(9), 4185–4190.
169 L. D. Field, S. A. Walper, K. Susumu, G. Lasarte-Aragones, E. Oh, I. L. Medintz and J. B. Delehanty, *Bioconjugate Chem.*, 2018, **29**, 2455–2467.
170 M. Raoufi, M. J. Hajipour, S. M. Kamali Shahri, I. Schoen, U. Linn and M. Mahmoudi, *Nanoscale*, 2018, **10**, 1228–1233.
171 L. X. Gao, H. Hao, Y. Q. Yu, J. L. Chen, W. Q. Chen, Z. D. Gong, Y. Liu and F. L. Jiang, *Langmuir*, 2023, **39**, 15275–15284.
172 A. C. G. Weiss, K. Krüger, Q. A. Besford, M. Schlenk, K. Kempe, S. Förster and F. Caruso, *ACS Appl. Mater. Interfaces*, 2019, **11**, 2459–2469.
173 P. L. Latreille, J. M. Rabanel, M. Le Goas, S. Salimi, J. Arlt, S. A. Patten, C. Ramassamy, P. Hildgen, V. A. Martinez and X. Banquy, *Adv. Mater.*, 2022, **34**(38), 2203354.

174 M. Germain, F. Caputo, S. Metcalfe, G. Tosi, K. Spring, A. K. O. Åslund, A. Pottier, R. Schiffelers, A. Ceccaldi and R. Schmid, *J. Controlled Release*, 2020, **326**, 164–171.
175 D. Sahoo, P. Bhattacharya, H. K. Patra, P. Mandal and S. Chakravorti, *J. Nanoparticle Res.*, 2011, **13**, 6755–6760.
176 M. S. Jahan Sajib, P. Sarker, Y. Wei, X. Tao and T. Wei, *Langmuir*, 2020, **36**, 13356–13363.
177 S. M. Kelly, T. J. Jess and N. C. Price, *Biochim. Biophys. Acta, Proteins Proteomics*, 2005, **1751**, 119–139.
178 B. A. Wallace, *Q. Rev. Biophys.*, 2009, **42**, 317–370.
179 C. Ge, J. Du, L. Zhao, L. Wang, Y. Liu, D. Li, Y. Yang, R. Zhou, Y. Zhao, Z. Chai and C. Chen, *Proc. Natl. Acad. Sci. U. S. A.*, 2011, **108**, 16968–16973.
180 D. Sanchez-Guzman, G. Giraudon-Colas, L. Marichal, Y. Boulard, F. Wien, J. Degrouard, A. Baeza-Squiban, S. Pin, J. P. Renault and S. Devineau, *ACS Nano*, 2020, **14**, 9073–9088.
181 L. Calzolai, F. Franchini, D. Gilliland and F. Rossi, *Nano Lett.*, 2010, **10**, 3101–3105.
182 P. S. Kumagai, A. P. U. Araujo and J. L. S. Lopes, *Biophys. Rev.*, 2017, **9**, 517–527.
183 B. A. Wallace, *Nat. Struct. Biol.*, 2000, **7**, 708–709.
184 D. Zhang, O. Neumann, H. Wang, V. M. Yuwono, A. Barhoumi, M. Perham, J. D. Hartgerink, P. Wittung-Stafshede and N. J. Halas, *Nano Lett.*, 2009, **9**, 666–671.
185 A. Kudelski, *Talanta*, 2008, **76**, 1–8.
186 C. Zong, M. Xu, L.-J. Xu, T. Wei, X. Ma, X.-S. Zheng, R. Hu and B. Ren, *Chem. Rev.*, 2018, **118**, 4946–4980.
187 I. Kuschnerus, K. Giri, J. Ruan, Y. Huang, N. Bedford and A. Garcia-Bennett, *J. Colloid Interface Sci.*, 2022, **612**, 467–478.
188 C. Zhang, Z. Jin, B. Zeng, W. Wang, G. Palui and H. Mattoussi, *J. Phys. Chem. B*, 2020, **124**, 4631–4650.
189 A. L. Ginzburg, L. Truong, R. L. Tanguay and J. E. Hutchison, *ACS Nano*, 2018, **12**, 5312–5322.
190 M. Assfalg, L. Ragona, K. Pagano, M. D'Onofrio, S. Zanzoni, S. Tomaselli and H. Molinari, *Biochim. Biophys. Acta, Proteins Proteomics*, 2016, **1864**, 102–114.
191 O. Cala, F. Guillière and I. Krimm, *Anal. Bioanal. Chem.*, 2014, **406**, 943–956.
192 M. Lundqvist, I. Sethson and B.-H. Jonsson, *Langmuir*, 2004, **20**, 10639–10647.
193 B. Hu, C. Wang, B. Chen and M. He, *ACS Nano*, 2021, **15**, 3108–3122.
194 M. Dolci, Y. Wang, S. W. Nooteboom, P. E. D. Soto Rodriguez, S. Sánchez, L. Albertazzi and P. Zijlstra, *ACS Nano*, 2023, **17**, 20167–20178.
195 M. C. Lo Giudice, L. M. Herda, E. Polo and K. A. Dawson, *Nat. Commun.*, 2016, **7**, 1–10.
196 X. Tan and K. Welsher, *Angew. Chem., Int. Ed.*, 2021, **60**, 22359–22367.
197 Y. Niu, Y. Yu, X. Shi, F. Fu, H. Yang, Q. Mu, D. Crespy, K. Landfester and S. Jiang, *Nano Lett.*, 2024, **24**, 9202–9211.